Accepted Manuscript

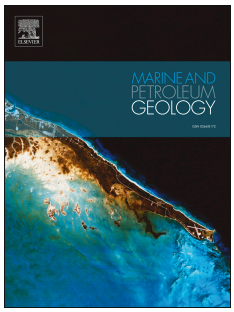

Diagenesis in salt dome roof strata: Barite - Calcite assemblage in Jebel Madar, Oman

Veerle Vandeginste, Manuela C. Stehle, Anne-Lise Jourdan, Harold J. Bradbury, Christina Manning, John W. Cosgrove

PII: S0264-8172(17)30215-5

DOI: 10.1016/j.marpetgeo.2017.06.008

Reference: JMPG 2942

To appear in: *Marine and Petroleum Geology*

Received Date: 7 February 2017

Revised Date: 6 June 2017

Accepted Date: 6 June 2017

Please cite this article as: Vandeginste, V., Stehle, M.C., Jourdan, A.-L., Bradbury, H.J., Manning, C., Cosgrove, J.W., Diagenesis in salt dome roof strata: Barite - Calcite assemblage in Jebel Madar, Oman, *Marine and Petroleum Geology* (2017), doi: 10.1016/j.marpetgeo.2017.06.008.

Diagenesis in salt dome roof strata: barite - calcite assemblage in Jebel Madar, Oman

Veerle Vandeginste[1,2,*], Manuela C. Stehle[1], Anne-Lise Jourdan[3], Harold J. Bradbury[1], Christina Manning[4], John W. Cosgrove[1]

[1]*Qatar Carbonate and Carbon Capture Research Centre and Department of Earth Science and Engineering, Imperial College London, Prince Consort Road, London, SW7 2BP, UK*

[2]*GeoEnergy Research Centre and School of Chemistry, University of Nottingham, University Park, NG9 2RD Nottingham, UK*

[3]*Bloomsbury Environmental Isotope Facility, UCL Earth Sciences, University College London, Gower Street, London, WC1E 6BT, UK*

[4]*Royal Holloway University of London, Dept. of Earth Science, Egham Hill, TW20 0EX, UK*

**Corresponding author: veerle.vandeginste@nottingham.ac.uk*

Abstract

Halokinesis causes a dynamic structural evolution with the development of faults and fractures, which can act as either preferential fluid pathways or barriers. Reconstructing reactive fluid flow in salt dome settings remains a challenge. This contribution presents for the first time a spatial distribution map of diagenetic phases in a salt dome in northern Oman. Our study establishes a clear link between structural evolution and fluid flow leading to the formation of diagenetic products (barite and calcite) in the salt dome roof strata. Extensive formation of diagenetic products occurs along NNE-SSW to NE-SW faults and fractures, which initiated during the Santonian (Late Cretaceous) and were reactivated in the Miocene, but not along the E-W fault, which was generated during Early Paleocene time. We propose that the diagenetic products formed by mixing of a warm (100ºC) saline (17 wt%

NaCl eq.) ^{87}Sr enriched ($^{87}Sr/^{86}Sr$: 0.71023) fluid with colder (35ºC) meteoric fluid during Miocene to Pleistocene. The stable sulphur and strontium isotope composition and fluid inclusion data indicate that a saline fluid, with sulfate source derived from the Ara Group evaporite and Haima Supergroup layers, is the source for barite formation at about 100ºC, predominantly at fault conjunctions and minor faults away from the main graben structure in the dome. In the Miocene, the saline fluid probably ascended along a halokinesis-related fault due to fluid overpressure (due to the rising salt and impermeable layers in the overlying stratigraphic sequence), and triggered the formation of barite due mixing with barium-rich fluids, accompanied by a drop in temperature. Subsequently, evolving salt doming with associated fault activity and erosion of the Jebel allows progressively more input of colder meteoric fluids, which mix with the saline warmer fluid, as derived from stable isotope data measured in the progressively younger barite-associated calcite, fault zone calcite and macro-columnar calcite. The reconstructed mixing model indicates a 50/50 to 90/10 meteoric/saline fluid mixing ratio for the formation of fault zone calcite, and a 10 times higher concentration of carbon in the saline fluid end member compared to the meteoric fluid end member. The presented mixing model of salt-derived fluids with meteoric fluids is suggested to be a general model applicable to structural diagenetic evolution of salt domes world wide.

Keywords: diagenesis; halokinesis; salt; barite; isotopes; mixing

1. Introduction

Coupling reactive fluid flow with structural deformation in rocks overlying and surrounding salt bodies remains a challenge. We still need to improve our understanding of how dynamic deformation, fluid-rock interaction, and resulting changes in permeability and rock texture, are impacted by thermal and fluid salinity gradients linked to the presence of salt. Such knowledge is important for accurate

predictions in hydrocarbon exploration and safe long-term CO_2 storage. Rock salt has played an important role in hydrocarbon exploration, due to its sealing capacity and its potential for forming trapping structures such as folds and faults. Similarly, rock salt is currently considered as a seal for CO_2 storage reservoirs. Hence, this sedimentary rock type is important in applications that represent effective solutions to combat climate change, crucial to our society.

Besides its potential as sealing layer (Wang et al., 2015; Yang et al., 2015), rock salt is characterized by a low density and visco-elastic behavior compared to other sedimentary rock types, which makes salt prone to flow when denser layers overlie the lower density salt layers or due to tectonic stress. Salt flow generates deformation of the surrounding rocks, hence, the importance of salt tectonics in hydrocarbon exploration (Archer et al., 2012). Applying seismic acquisition to image salt diapirs is very challenging due to the strong acoustic impedance and velocity contrasts at the sediment – evaporite interface and complex shapes of steeply dipping flanks (Hudec and Jackson, 2007). Nevertheless, advances in structural models in salt tectonics have been achieved through sandbox experiments, theoretical models and field examples (Jackson and Vendeville, 1994; Vendeville, 2005; Yin and Groshong, 2007; Yin et al., 2009), fluid flow models (Evans et al., 1991; Gradmann et al., 2012; Holzbecher et al., 2010; Ranganathan, 1992; Ranganathan and Hanor, 1989; Sarkar et al., 1995; Williams and Ranganathan, 1994; Wilson and Ruppel, 2007), and 3-dimensional seismic datasets (Gamboa and Alves, 2016; Jackson and Lewis, 2016; Mattos et al., 2016; Omosanya and Alves, 2013).

Salt domes studied at the surface provide excellent opportunities to collect field data that can be used subsequently as input feed or benchmarking for models. For example, a study that documents in detail the spatial distribution of fluid types and precipitation temperature of vein cements along La Popa salt weld in NE Mexico (Smith et al., 2012) is one of the few investigations published on the integration of

structures and reactive fluid flow in salt dome settings. A study on core samples from the Scotian Basin has also reported that active detachment faults on salt welds provide potential pathways and a source of salt for migrating formation water, leading to barite and sphalerite formation (Pe-Piper et al., 2015). A wide assemblage of diagenetic products can be found in salt dome cap rocks (Hallager et al., 1990). Barite is often a minor component among other minerals such as abundant metal sulphides, carbonates and elemental sulphur (Bechtel et al., 1996; Morrison and Parry, 1986; Sassen et al., 1994; Saunders and Thomas, 1996). Barite formation can be triggered as replacement of anhydrite by a decrease in temperature (Wagner et al., 2005), or by mixing of barium-rich fluids with sulphate-bearing fluids (Feng and Roberts, 2011; Greinert et al., 2002; Hanor, 2000; Tombros et al., 2015; Torres et al., 2003).

In the current paper, we report the study of structurally-controlled diagenesis in carbonate strata overlying a salt diapir in Jebel Madar (northern Oman). This salt dome in the Foothills of the central Oman Mountains is an excellent field site to investigate the evolution of paleofluid migration related to dynamic structural development during halokinesis, because of its great exposure, relatively easy access, extensive occurrence of diagenetic products (in particular barite and calcite), and the fact that it is not a surface-piercing salt dome (the salt does not occur in outcrop). The main objectives of this contribution are the following: (1) to document the spatial distribution of structurally-controlled diagenetic products in salt dome roof strata, (2) to determine the texture and geochemical signatures of the diagenetic products and paleofluids in salt dome roof strata, and (3) to link the paleofluid migration with structural evolution during halokinesis and reconstruct diagenetic product formation conditions. The integration of these datasets, with particular focus on the abundant presence of large barite crystals which have not been previously reported, combined with literature data, provides the reconstruction of diagenetic fluid migration in dynamic structural settings impacted by halokinesis.

2. Geological setting

Jebel Madar is a dome shaped, 500m-high mountain with an elliptical outline of 5 by 8 km, and is situated in the Adam Foothills, south of the central Oman Mountains in Northern Oman (Fig. 1). The Jebel formed by diapirism of the Precambrian-Cambrian Ara salt (Mount et al., 1998) of the Ghaba Salt Basin. The Ghaba, Fahud and South Oman Salt Basins form the three evaporitic basins that are present in the deep subsurface of Interior Oman (Allen, 2007; Reuning et al., 2009). These basins are NE-SW oriented, and are interpreted to follow left-lateral, strike-slip faults in the basement (Loosveld et al., 1996). The Ara Salt was deposited coeval with the Hormuz Salt in Iraq, Iran, Kuwait and Pakistan (Allen, 2007; Edgell, 1991). The timing of diapirism is not well constrained, but it has been linked to separate events such as the initiation of ophiolite emplacement in the Late Cretaceous (Farzadi, 2006), or tilting of the eastern flanks of the salt basins during the Miocene Alpine compressional phase (Terken et al., 2001). Alternatively, a combination of events may have led to diapirism, with potentially minor salt movement having started in the Late Jurassic and followed by accelerated diapirism associated with the ophiolite obduction and the Alpine Orogeny (Ericsson et al., 1998; Peters et al., 2003). Still, the main doming event of Jebel Madar is probably linked with the Alpine Orogeny and thus of Miocene age (Claringbould et al., 2013).

The Late Neoproterozoic to Early Cambrian Ara Group consists of marine platform sediments representing at least six third-order cycles of carbonate to evaporite sedimentation (Schoenherr et al., 2010). These cycles are formed by Ara salt sedimentation at shallow depth followed by isolated platform carbonate deposits in deeper basins during transgression (Mattes and Morris, 1990). The Ara evaporite in the core of Jebel Madar dome consists mainly of halite, anhydrite which replaced primary gypsum (Mattes and Morris, 1990), and minor amounts of potash salts and Mg sulphates (Schroder et al., 2003).

The lithologies of the roof strata at Jebel Madar consist mainly of carbonate of Triassic to early Cretaceous age, belonging to the Hajar Supergroup (Fig. 2). This Supergroup consists of the Akhdar, Sahtan, Kahmah and Wasia Groups (Béchennec et al., 1993). The oldest formations, the Triassic Akhdar Group dolostone and Jurassic Sahtan Group sandstone and limestone crop out in the center of the Jebel, at a triple junction between the main faults (which created the Southwest Gully, East Gully and Sheep Valley), whereas the main part of the Jebel exposes Cretaceous Formations (Fig. 2). The Lower Cretaceous Kahmah Group consists of the Rayda, Salil, Habshan, Lekhwair, Kharaib and Shuaiba Formations. The three oldest formations in this Group form a prograding sequence of shallowing-upward facies with distal slope mudstone (shaly limestone and marls) of the Salil Formations, mid-ramp shoal ooidal and bioclastic grainstone and packstone of the Habshan Formation and inner platform algal mudstone, wackestone, bioclastic-peloidal grainstone and rudist-bearing packstone and floatstone of the Lekhwair Formation (Droste and van Steenwinkel, 2004). The latter is overlain by inner platform bioturbated, bioclastic (rudist-bearing) and peloidal packstone of the Kharaib Formation and (on top) the Shuaiba Formation. The Wasia Group comprises the Nahr Umr Formation, composed of shales and lime mudstones, and the Natih Formation with interfingering carbonate platform and intrashelf basin deposits of thickly-bedded mudstone, bioturbated wackestone, packstone and grainstone with abundant rudists and *Thalassinoides* burrows (Droste and van Steenwinkel, 2004).

The main formation of the Oman Mountains took place during the Alpine Orogeny Phase 2 (Eocene to Pliocene), whereas the area was earlier affected by the obduction of Semail ophiolite during Alpine Phase 1 (Turonian to Lower Maastrichtian) (Claringbould et al., 2013; Glennie, 2005; Gomez-Rivas et al., 2014; Mann and Hanna, 1990). The exact amount of burial underneath the Hawasina thrust sheets at the site of Jebel Madar is not accurately known, but was estimated at 1km by Claringbould et al. (2013) based on seismic sections from within a ten km range

from Jebel Madar. A detailed structural and stratigraphic map of Jebel Madar is presented by Claringbould et al. (2013). Other previous work on Jebel Madar documents dolomitization in the Habshan Formation (Vandeginste et al., 2013a) and Pleistocene phreatic calcite cave deposits (Immenhauser et al., 2007). The dominant calcite and barite diagenetic phases described in the current contribution occur mainly along previously mapped faults and fractures (Claringbould et al., 2013); only very small occurrences are more dispersed in the host rock or found in small patches or veins.

3. Methodology

For mapping the occurrence of barite and calcite cements along faults and fractures or in large vugs or caverns, we made use of Google Earth maps, the geological map of Claringbould et al. (2013), and a handheld Garmin Oregon GPS unit. GPS locations were recorded for our tracks, collected samples and structural measurements. A total of 249 hand samples were collected for this study, and a total of 154 structural measurements (including strike and dip of fractures and faults) using a Brunton compass.

Hand samples were cut, polished, etched with 1M HCl and stained with Alizarin Red S and potassium ferricyanide to distinguish calcite from other minerals (in particular dolomite and barite) following a procedure modified from Dickson (1966). Samples that were not identified as calcite by red or purple staining were subjected to X-ray diffraction analysis to determine the mineralogy, in particular to verify barite and detect potential presence of celestite (or lack thereof).

A total of 66 thin sections were examined using a Zeiss Axioskop 40 polarization microscope (with a connected Zeiss Axiocam ICc1 digital camera for photomicrographs) and a CITL cathodoluminescence (CL) Mk5-2stage mounted on a Nikon Eclipse 50i microscope (with an attached Nikon DS-Fi1c digital camera). Operating conditions for the CL stage were about 200 µA and 13 kV.

For elemental analysis, sample powders of pure calcite and host rock were prepared by crushing small pieces of rock (cleaned with distilled water and dried overnight) using an agate mortar and pestle. An aliquot of 200 mg of each sample powder (144 in total) was dissolved in 50 mL of a 5% HNO_3 solution (Vandeginste et al., 2013b). Analytical precision at the 95% confidence level determined on replicate analyses is about 15% for Ca, Mg, Al and Sr, and 10% for Fe and Mn.

Stable carbon and oxygen isotope analyses were carried out on more than 200 carbonate samples. Aliquots of about 100 to 150 µg were reacted with phosphoric acid in a Thermo Scientific automated Kiel IV carbonate device at 70ºC, and the resulting CO_2 gas was analysed in a MAT253 mass spectrometer. The carbon and oxygen isotopic values for carbonate samples are reported in per mil notation relative to Vienna Peedee belemnite (VPDB). Replicate analysis of NBS19 and Carrara Marble internal lab standards determined reproducibility better than 0.03‰ (1σ) for $\delta^{13}C$ and 0.06‰ (1σ) for $\delta^{18}O$. Triplicates of samples show sample heterogeneity of 0.13‰ (1σ) for $\delta^{13}C$ and 0.12‰ (1σ) for $\delta^{18}O$.

Aliquots of 0.9 mg of barite were weighed and placed in silver capsules, and the oxygen isotopic composition was measured on a TC/EA pyrolysis-coupled IRMS Delta Plus XP Thermofisher at CCiT at the University of Barcelona. Reproducibility of the oxygen isotope analysis is 0.2‰ (1σ, n = 2). Sulphur isotopes on barite samples were analysed by IsoAnalytical using EA-IRMS. The reference material used for analysis was IA-R061 (Iso-Analytical working standard barium sulphate, $\delta^{34}S_{VCDT}$ = +20.3‰). Repeated analysis of standard IA-R061 has a precision of 0.2‰ (1σ, n = 3) and repeated analysis of internal standard IAEA-SO-5 has a precision of 0.06‰ (1σ, n = 3).

For Sr isotope analyses, the pure calcite samples were dissolved in ~1mL dilute HNO_3. Barite samples were leached in 6M HCl overnight, evaporated, and then dissolved in 2.5M HCl following the analytical procedure by Marchev et al. (2002).

Strontium was separated from the solutions using Eichrom Sr-spec resin, and analysed on a VG354 thermal ionization mass spectrometer at Royal Holloway University of London (UK). Samples were loaded on single Re filaments with a TaF emitter, and run using the multidynamic procedure of Thirlwall (1991). The SRM987 standard ran with the samples gave a mean value of 0.710256±0.000009 (1σ, N=9). Fluid inclusions were studied in doubly polished wafers of calcite and barite cements on a Linkam THMSG600 heating-cooling stage. Since most (>90%) fluid inclusions observed were single-phase, the wafers were placed in a freezer overnight to generate two-phase fluid inclusions, a method described by Goldstein and Reynolds (1994), which was successful for barite, but not for calcite. Two-phase fluid inclusions appeared to stretch during rapid heating-cooling sequences in calcite, and hence, no reliable homogenization temperatures could be determined in calcite. Reproducibility of the final melting temperature of ice (Tm) is within 0.2ºC for both calcite and barite, and that of the homogenization temperature (Th) of barite samples is within 2ºC. Inclusions in barite are susceptible to stretching and decrepitation during overheating (Ulrich and Bodnar, 1988). The barite minerals have not experienced higher temperature than the temperature they were formed at, given the indications for barite formation during halokinesis (and thus the uplift phase rather than burial). Overheating was avoided during microthermometric measurements by only heating each wafer piece till the homogenization temperature of the measured inclusions within that piece.

4. Macroscopic and petrographic characteristics of diagenetic products

4.1. Barite

Barite is found within host rock or co-occurs with barite-associated calcite within veins or large fractures. The host rock in which barite is found belongs to the Lekhwair (predominantly) and Kharaib formations. Typically, barite is present at the rim of the vein, whereas barite-associated calcite fills the inner space of the fractures

(Fig. 3A). Barite has generally tabular-shaped or lath-like euhedral crystals (of up to several centimeters wide), which are dispersed in the host rock (Fig. 3B) or more commonly form layers of radiating bundles (Fig. 3C). In some instances, barite is found as rosette structures of cross-cutting tabular crystals (Fig. 3D). Under crossed polarized light, barite is distinguished by its lower interference colours than that of calcite. Some fan-shaped barite crystals have sweeping extinction, but the lath-shaped crystals have homogeneous extinction. Bedding-parallel stylolites cross-cut the host rock and barite laths, but not the inclusion-poor barite-associated calcite. Calcite fills fractures within barite crystals (Fig. 4A-B). Barite is non-luminescent when viewed with the CL microscope.

4.2. Calcite

Four types of calcite have been distinguished in this study based on their occurrence and characteristics, 1) thin calcite veins, 2) barite-associated calcite, 3) fault zone calcite, and 4) macro-columnar calcite. The first type of calcite occurs in thin (up to a few centimeters thick) veins within the host rock (Fig. 5A). These calcites have a crystal size < 1 cm and are blocky in shape.

The second type of calcite is present in meter-scale barite patches and in fractures that contain barite (Fig. 5B). Here, calcite fills space between the tabular barite crystals or they grow in the center of fractures on top of radiating barite crystals. In some diagenetic occurrences, calcite dominates over barite, and in those instances, barite forms small patches within larger calcite zones. Barite-associated calcite is crosscut by reddish brown silt (Fig. 6A) and macro-columnar calcite. The calcite crystals have homogeneous extinction and some contain two cross-cutting sets of faint, thick, cleavage twin planes, whereas other crystals have none or only fine, thin, cleavage twin planes. The latter crystals are in general light coloured and contain few inclusions. Under CL, calcite has a dull orange luminescence, commonly with lighter

279 and darker coloured zonations (Fig. 4B). Inclusion-free calcite is dull orange
280 luminescent and cuts through barite.
281 The third type of calcite occurs as large calcite crystals of up to tens of centimeters
282 long along major faults (Fig. 5C). These crystals are transparent and some have a
283 faint white or greenish colour. In thin section, this calcite has relatively thick cleavage
284 twinning planes (Fig. 4C) and a CL pattern of darker and lighter orange zonations
285 (Fig. 4D).
286 The fourth type of calcite, macro-columnar calcite, is recognized in the field by its
287 transparent crystals that can contain reddish colored zones (Fig. 5D) or co-occur with
288 reddish brown silt layers (Fig. 6B). These crystals are generally a few, up to tens of
289 centimeters long, and are commonly macro-columnar in shape, occasionally forming
290 a radiating pattern (Fig. 5E). There are also white calcite rosettes which are topped
291 by a reddish, thin layer (Fig. 5F). These rosettes grow upwards and are stacked upon
292 each other, leaving some pore space in between them. The crystals in these
293 structures are up to 5 cm long. The macro-columnar calcite has inclusion-poor calcite
294 crystals (Fig. 4E) that display an inhomogeneous extinction pattern under crossed
295 polarized light. The calcite is mainly non-luminescent under CL, but also displays
296 some thin, dull orange luminescent zonations (Fig. 4F). Large veins filled with macro-
297 columnar calcite crosscut fault zone calcite. Extensive calcite zones exhibit cross-
298 cutting of multiple veins within larger vein zones, whereby the vein cement
299 crosscutting all other vein cements is of the macro-columnar type with transparent
300 and reddish crystal colour (Fig. 6C-E).
301

302 **5. Spatial distribution of barite and calcite types**

303 The distribution of barite and significant calcite type occurrences was mapped in
304 Jebel Madar (Fig. 7). Most of the calcite mineralization is found near the three large
305 structures (connected with each other in the center at the triple junction), whereas
306 almost no mineralization apart from thin veins are found close to the rims of Jebel

Madar. The structural orientation of the fractures filled with different diagenetic products shows that the NNE-SSW to NE-SW trend is dominant and a second, NW-SE trend is of minor importance (Fig. 8). Both structural trends are represented in thin veins, but the larger structures with barite-associated calcite, fault zone calcite and macro-columnar calcite generally exhibit the dominant, NNE-SSW to NE-SW trend. Fractures filled with barite and barite-associated calcite are mainly NE-SW oriented, whereas the highest distribution of structures containing fault zone calcite and macro-columnar calcite is in NNE-SSW oriented fractures.

Barite is rare along the main, Southwest Gully NE-SW graben structure of the southwestern part of Jebel Madar, but is concentrated along other faults in the southern part of the Jebel (Hawk Valley) and three other occurrences slightly further away from the three main faults, especially where (minor) faults intersect (Fig. 7). There is a high concentration of macro-columnar calcite in an intensely fractured zone and cavern in the Shuaiba Formation in the southwestern corner of Jebel Madar (Sarg Valley), but some macro-columnar calcite also occurs along the main, Southwest Gully, NE-SW graben structure (mainly in the Shuaiba Formation), and is rare along faults in the northern (and northeastern) part of the Jebel (Sheep Valley and East Gully).

6. Geochemical data of diagenetic products

6.1. Stable carbon, oxygen, sulphur and strontium isotope geochemistry

The stable isotopic signature of limestone, barite and the different calcite types is presented in Supplementary File Table 1. The barite $\delta^{18}O$ signature is between +19.8 and +25.4‰ VSMOW; the $\delta^{34}S$ of most barite samples falls between +27.0 and +37.6‰ VCDT, but two samples have a $\delta^{34}S$ value of +47.9 and +48.8‰ VCDT (Fig. 9, Supplementary File Table 1). For the stable isotope composition in the calcite types, both the average $\delta^{13}C$ and $\delta^{18}O$ (in ‰ VPDB) decrease in the following order:

334 from barite-associated calcite ($\delta^{13}C$ = +2.8 ± 0.5 and $\delta^{18}O$ = -4.5 ± 1.2), to thin calcite
335 veins ($\delta^{13}C$ = +2.5 ± 1.2 and $\delta^{18}O$ = -4.8 ± 1.8), to fault zone calcite ($\delta^{13}C$ = +0.5 ± 1.0
336 and $\delta^{18}O$ = -11.0 ± 1.3), and finally to macro-columnar calcite ($\delta^{13}C$ = -5.5 ± 1.4 and
337 $\delta^{18}O$ = -14.0 ± 0.8; Fig. 10, Supplementary File Table 1). From barite-associated
338 calcite and thin calcite veins to fault calcite, the decrease in $\delta^{18}O$ of about 6‰
339 dominates (compared to 2‰ for $\delta^{13}C$), whereas from fault calcite to macro-columnar
340 calcite, the decrease in $\delta^{13}C$ of about 6‰ (compared to 3‰ for $\delta^{18}O$) is dominant
341 (Fig. 10).
342 The average $^{87}Sr/^{86}Sr$ ratios decrease from barite (0.71044 ± 0.00055), to barite-
343 associated calcite (0.71000 ± 0.00067), to thin calcite veins (0.70991 ± 0.00078), to
344 fault zone calcite (0.70935 ± 0.00009) and to macro-columnar calcite (0.70894 ±
345 0.00008; Supplementary File Table 1; Fig. 11). This order is similar as observed for
346 the trend in the stable oxygen and carbon isotope values. The spread in $^{87}Sr/^{86}Sr$
347 ratios between samples of the same phase is small for macro-columnar and fault
348 zone calcite compared to the other calcite types. The limestone samples show a wide
349 range in $^{87}Sr/^{86}Sr$ data and the average value (0.70955 ± 0.00038) falls between that
350 of fault zone calcite and that of thin calcite veins (Supplementary File Table 1).
351
352 *6.2. Major and minor element geochemistry*
353 The elemental content does not vary distinctly between different calcite types
354 (Supplementary File Table 2). There is a weak positive correlation between Sr and
355 Mg content, and the elemental composition of the different calcite types is similar for
356 these two elements (Fig. 12A). The Ba content is highly variable among samples and
357 the highest average values are obtained in the calcite cement and Kharaib Formation
358 limestones, whereas the Shuaiba Formation limestones have the lowest average Ba
359 content (Supplementary File Table 2). The main element that shows a clear trend
360 between diagenetic phases is Mn, with a decreasing average content from barite-

associated calcite (187 ± 66 ppm), to thin calcite veins (151 ± 75 ppm) to fault zone calcite (128 ± 26 ppm) and to macro-columnar calcite (59 ± 55 ppm; Fig. 12B).

6.3. Fluid inclusion study

Barite as well as the calcite types studied contain mainly single-phase liquid inclusions of about 3 by 5 to 7 by 10 µm large (Fig. 13). Homogenization temperature of generated two-phase primary fluid inclusions (after putting wafer in freezer) in barite ranges from 82 to 123ºC (Supplementary File Table 3; Fig. 14A). Salinity in interpreted primary fluid inclusions, derived from final ice melting temperatures using the equation of Goldstein and Reynolds (1994) is around 21 wt% NaCl eq in barite, and decreases in the different calcite types, from 17 wt% NaCl eq in barite-associated calcite, to 2 to 4 wt% NaCl eq in two samples of fault-zone calcite, to 0.1 wt% NaCl eq in macro-columnar calcite (Fig. 14B). The salinity in the calcite types shows a positive correlation with the $\delta^{18}O$ values of the calcite samples measured, i.e. higher salinity corresponds to higher $\delta^{18}O_{calcite}$ values (Fig. 14B). First hydrous salt melting temperatures in barite between -53 and -45ºC indicate a saline aqueous system with predominantly $CaCl_2$, whereas the first hydrous salt melting temperature in fluid inclusions in barite-associated calcite between -34 and -23ºC (Supplementary File Table 3) indicate a saline system dominated by NaCl with minor addition of KCl and $CaCl_2$.

7. Discussion

7.1. Diagenetic barite-calcite assemblage in salt dome roof strata

Diagenetic products in strata overlying a salt diapir are likely to be influenced by the presence of the salt as well as by the structural deformation related to the halokinesis (Archer et al., 2012). Previous diagenetic work on five sampling sites in Jebel Madar concentrated mainly on phreatic cave deposits with macro-columnar calcite,

388 identified traces of barite, and included some fault zone calcite (Immenhauser et al.,
389 2007). The novelty in our study involves the exploration of the entire Jebel to
390 document the spatial distribution of all diagenetic phases present in the strata
391 overlying the salt diapir, as observed in outcrop, with an important focus on
392 significant barite occurrences, and the link to structures (Fig. 7).
393 We distinguished different diagenetic cements, i.e. barite and several calcite types,
394 based on their mineralogy and textural and geochemical characteristics. The
395 abundance of large barite crystals in Jebel Madar has not been previously reported.
396 In contrast to calcite, which is a common diagenetic product in sedimentary strata,
397 barite (barium sulphate) is more rare, but not uncommon in salt dome settings
398 (Warren, 2000). Salt diapirs are often overlain by a caprock consisting of an
399 anhydrite zone and overlying carbonate zone with anhydrite, gypsum, elemental
400 sulphur, metal sulphides such as pyrite, sphalerite and galena, and Sr and Ba
401 minerals such as barite, celestite and strontianite (Sassen et al., 1994; Saunders and
402 Thomas, 1996; Souissi et al., 2007).
403 Barite occurring in the roof strata of the Jebel Madar salt dome has large (up to
404 centimeter scale) crystals, which have a rhombohedral, tabular shape, present as
405 single lath-shaped crystals, as radiating bundles organized in layers separated by
406 thin dark coatings, or as rosettes. The rhombohedral morphology suggests that the
407 barite formed via surface reaction growth mechanisms from a solution with a low
408 degree of barite saturation, in contrast to highly saturated fluids which favour the
409 precipitation of dendritic (rod-like, spindle-like, star-like) barite crystals by diffusional
410 transport (Dunn et al., 1999; Shikazono, 1994). The barite rosettes indicate growth in
411 open space, as they are still present in cavities, which is consistent with growth in
412 extensional fault zones (Balsamo et al., 2016).
413 The large size of the barite crystals contrasts strongly with the micrometer scale of
414 marine pelagic barite (Bertram and Cowen, 1997; Dehairs et al., 1980; Griffith and
415 Paytan, 2012), and indicates formation at elevated temperature, as confirmed by fluid

inclusion microthermometric data (> 80ºC). We must note, though, that the fluid inclusion homogenization temperature data in barite need to be treated with caution. Barite has good cleavage and a low bulk modulus and often contains single-phase fluid inclusions alongside two-phase inclusions, even for formation conditions at 150ºC, and this may be caused by overpressuring of fluids in the inclusions linked to post-entrapment deformation of barite (Badhe and Pandalai, 2015). Nevertheless, in addition to the barite crystal morphology and size and the formation temperature of about 110ºC of barite-associated calcite (see below), it can be concluded that barite formed at elevated temperature.

Crosscutting relationships indicate that barite is older than the documented calcite types, and that macro-columnar calcite is younger than fault zone calcite, itself postdating barite-associated calcite (Fig. 3, 5-6, 15). The type and diversity of diagenetic products forming in the neighbourhood of salt diapirs relate to the diagenetic process involved, determined by the setting, such as migrating fluids, host rock, and temperature. The presence of barite and the lack of sulphides suggest predominance of sulphate over sulphide implying the lack of or very limited sulphate reduction, a process common in settings containing organic-rich sediments with sulphate-reducing bacteria or hydrocarbons (Cai et al., 2005; Machel, 2001; Vandeginste et al., 2006; Vandeginste et al., 2009).

7.2. Paleofluid flow pathways and evolution through time

The abundant large diagenetic products present within the faults and fractures in the dome testify to the important role of these structures as preferential fluid pathways. Fault zones have also been documented to be major fluid pathways in other jebels in the Adam Foothills in northern Oman (Mozafari et al., 2015). The stress field that controlled and generated the faults and fractures in the carbonate strata overlying the salt diapir in Jebel Madar is thought to be controlled both by the local stress field linked to salt diapirism itself, as well as to regional tectonics (Claringbould et al.,

444 2013; Quinta et al., 2012). The paragenesis of the cement types (Fig. 15) can thus
445 reveal information on the evolution of structures during halokinesis and the interplay
446 between regional tectonics and local stress caused by salt doming.
447 The orientation of thin calcite veins is variable, but the dominant orientation of barite-
448 associated calcite structures (NE-SW) is similar to that of structures filled with fault
449 zone calcite and macro-columnar calcite (NNE-SSW). Hence, the NE-SW to NNE-
450 SSW structures were the main pathways for fluids from which the diagenetic
451 products formed. In contrast, no significant occurrence of diagenetic products was
452 observed along the E-W fault, suggesting lack of fluid migration along E-W
453 structures. The orientation of the main structures and also the shape of Jebel Madar
454 indicate that the NE-SW trend dominated the elongated dome shape and the normal
455 faulting during halokinesis. This NE-SW trend is interpreted to relate to pre-existing
456 normal faults of Precambrian age present in the basement, which probably also
457 controlled the location of the diapir (Claringbould et al., 2013; Immenhauser et al.,
458 2007).
459 Despite the challenges in the interpretation of the major structures in Jebel Madar,
460 Claringbould et al. (2013) suggests that the development of the structures occurred
461 in three phases: 1) Late Cretaceous dome initiation and the formation of NE-SW
462 fractures followed by the development of grabens and cementation, 2) Early
463 Paleocene E-W dextral strike-slip faulting with lack of cementation, and 3) Miocene
464 reactivation and inversion of faults and a final period of diapirism and dome.
465 However, petrographic and geochemical (notably radiogenic dating) data from
466 macro-columnar calcite suggests that these cements were deposited during the
467 Pleistocene to Holocene (Immenhauser et al., 2007). Based on these previous
468 studies and the data presented in the current contribution, we propose that the
469 structural evolution follows that proposed by Claringbould et al. (2013), but that major
470 barite and calcite cementation only started in the Miocene and not in the Late
471 Cretaceous. Claringbould et al. (2013) interpreted down-dip slickenlines on calcite

fault surfaces as an argument to suggest abundant burial calcite cementation along NE-SW fault zones in Late Cretaceous time, and then reactivation of those faults in the Miocene. In contrast, we hypothesise that the NE-SW faults and fractures developed during Late Cretaceous time, but that abundant cementation occurred during reactivation and final dome formation during Miocene to Pleistocene times, during which several pulses and episodes of fluid flow and NE-SW fault reactivation occurred (Fig. 16).

Seismic sections and interpretations by Claringbould et al. (2013) show that salt doming has caused an uplift of about 2 to 2.5 km (in the centre of the dome). Reported salt diapirism induced uplift rates are in the order of 2 to 8 mm per year in the center of a dome (Bruthans et al., 2006; Pe'eri et al., 2004). These uplift rates suggest that salt diapirism in Jebel Madar causing 2 km uplift could have happened in about 250 to 1000 kyr. Since there are no outcrops of post-Natih Formation age, it can be argued that at least 1.5 km of material has been eroded either during or immediately after salt doming. High end values of denudation rates of about 0.1 mm per year (Kirchner et al. 2001) support erosion of a 1.5 km thick package in a time period of about 15 Myr. These calculations indicate that it is plausible that the diagenetic products resulted from fluid flow pulses along the major faults during dome formation in the last 15 million years. This model is supported by the Miocene to Pleistocene age of the cements, formed by mixing of fluids, as discussed below.

The spatial distribution of the diagenetic products elucidates further the sequence of cement precipitation along structures in the Jebel, and thus helps to reconstruct fluid migration during halokinesis. Fault zone calcite is present along each major fault, except for the NE-SW fault near Hawk Valley in the southern part of the Jebel, which is cemented by barite and barite-associated calcite (Fig. 7). Since the latter are the oldest diagenetic products in the paragenesis (Fig. 15), we interpret that fluid migration focused first along this Hawk Valley NE-SW fault. Only minor amounts of barite have been documented along the main, Southwest Gully, NE-SW graben

500 structure, where more focused fluid migration took place subsequently during
501 abundant formation of fault zone calcite. Macro-columnar calcite is present along NE-
502 SW faults (postdating fault zone calcite) and is especially abundant in the
503 southwestern zone (and previously documented eastern area) in Shuaiba Formation
504 host rock. Moreover, macro-columnar calcite has been documented in the Shuaiba
505 Formation away from the main faults in the eastern part of Jebel Madar
506 (Immenhauser et al., 2007). Hence, besides the structural control, there is also a
507 sedimentologic control at least on the spatial distribution of the macro-columnar
508 calcite. The abundance in the Shuaiba Formation relates to its stratigraphic position
509 underneath the Nahr Umr seal, as formation fluids were trapped and dissolution
510 affected the host rocks, causing solution-enhanced fractures and caverns due to
511 cooling of formation waters during halokinesis-induced uplift before cementation
512 (Immenhauser et al., 2007).
513 In conclusion, cementation occurs first from fluids (generating barite and barite-
514 associated calcite) focused along minor faults and conjunctions at sites several
515 kilometers apart spread within the Jebel, subsequently from fluids along NE-SW
516 faults with abundant fault-zone calcite precipitation along the major NE-SW fault, and
517 finally from fluids focused mainly in the southwestern and eastern zone along NNE-
518 SSW to NE-SW structures and in the Shuaiba Formation, generating macro-
519 columnar calcite.
520
521 *7.3. Origin and formation process of barite*
522 Dissolution of evaporites is one of the main origins of subsurface brines in
523 sedimentary basins, besides subaerial evaporation of seawater and membrane
524 filtration (Hanor, 1994). The evaporites, such as anhydrite or other sulphate minerals,
525 at the core of a salt dome, are a likely source of sulphate for barite formation in this
526 setting, similar to examples in other studies where sulphates and sulphides formed in
527 evaporite settings (Warren, 2000). Jebel Madar formed in response to diapirism of

the Late Neoproterozoic to Early Cambrian Ara Group evaporite, consisting mainly of halite, anhydrite which replaced primary gypsum (Mattes and Morris, 1990), and minor amounts of potash salts and Mg sulphates (Schroder et al., 2003).

Fluid inclusion measurements indicate that barite and barite-associated calcite precipitated from highly saline fluids (21 and 17 wt% NaCl eq, respectively) probably at around 100ºC. Fluid inclusion measurements in barite need to be treated with caution, as mentioned above. Although the fact that the fluid inclusion assemblage is dominated by single-phase inclusions generally suggests a mineral formation temperature of less than 40 to 60ºC, it is not uncommon for small inclusions (< 3 µm) to be single-phase aqueous inclusions even though the homogenization temperature is as high as 100ºC (Goldstein and Reynolds, 1994). Clumped isotope data corroborate formation at burial conditions with a barite-associated calcite formation temperature of around 110ºC (John et al., 2014). Moreover, dissolution of anhydrite has been documented at about 110ºC based on reflectance data from pore-filling solid bitumen in caprock of the exposed salt domes in the Ghaba Salt Basin (Reuning et al., 2009).

Further supporting evidence for the elevated temperature formation of barite and barite-associated calcite is provided by the oxygen isotope geothermometer, assuming that the co-occurring calcite and barite formed under very similar conditions (similar fluid and temperature) and under equilibrium oxygen isotope fractionation. Taking the average oxygen isotope composition of barite (+22.8‰ VSMOW) and barite associated calcite (+26.3‰ VSMOW), we calculate a formation temperature of 90ºC and 115ºC, based on the oxygen isotope fractionation of barite – saline water (Kusakabe and Robinson, 1977) and of calcite – water from Friedman and O'Neil (1977) and Demeny et al. (2010), respectively:

$$1000 \ln \alpha_{cc\text{-}bar} = 0.14 \frac{10^6}{T^2} + 2.41$$

554 $$1000 \ln \alpha_{cc-bar} = -2.64 \frac{10^6}{T^2} + 17.599 \frac{10^3}{T} - 24.34$$

555 The sulphate source for barite formation is confirmed by sulphur isotope data. The
556 $\delta^{34}S$ in barite in Jebel Madar (+31 ± 3 ‰ VCDT) is typical for the sulphate
557 composition of Late Neoproterozoic to Early Cambrian seawater (Claypool et al.,
558 1980), suggesting that the source of sulphate was Ara Group evaporite. Seawater
559 and associated sulphate deposits of younger age are characterized by a much lower
560 $\delta^{34}S$ value (Claypool et al., 1980; Paytan et al., 2004; Rees et al., 1978). There is a
561 good match between the measured $\delta^{34}S$ values in barite of Jebel Madar and that in
562 Late Neoproterozoic to Early Cambrian anhydrite from Siberia and India (Banerjee et
563 al., 1998; Claypool et al., 1980; Strauss et al., 2001). Moreover, the barite data in this
564 study overlap both with the sulphur isotope values from anhydrite cements in the
565 Haima Supergroup in the Fahud Salt Basin, i.e. +20.4 to +30.6‰ VCDT (Ramseyer
566 et al., 2004) and those of the Ara Group anhydrite in the South Oman Salt Basin, i.e.
567 +32.4 to +46.4‰ VCDT (Schroder et al., 2004) and plot predominantly between the
568 averages of those datasets (Fig. 9). Schroder et al. (2004) invoked the process of
569 bacterial sulphate reduction to explain the elevated $\delta^{34}S$ signature in anhydrite in the
570 South Oman Salt Basin compared to the sulphate composition in Late
571 Neoproterozoic to Early Cambrian deposits from other parts of the world, based on
572 the presence of organic-rich source rocks underlying and interbedded with the Ara
573 Group evaporites (Mattes and Morris, 1990; Schoenherr et al., 2009), and source
574 rocks present in the Ghaba Salt Basin (Reuning et al., 2009). The sulphate origin of
575 barite in Jebel Madar thus represents a mixing of two sources: dissolved sulphate
576 from the Ara Group and from the Haima Supergroup.
577 The extensive occurrence of barite along faults in the salt dome, when considered in
578 concert with the identified source for sulphate, suggests that sulphate-rich fluids
579 preferentially migrated along halokinesis-related faults and fault conjunctions. The
580 driving force for the ascent of the fluids is not entirely certain. The pressure exerted

by the rising salt upon the overlying stratigraphic sequence, which includes impermeable layers such as shale units in the Haima Supergroup, the Haushi Group and the Nahr Umr Formation, can have led to fluid overpressure, and the release of those overpressured fluids during fault activity. Another potential scenario considers upward release of fluids linked to the decrease in overburden pressure due to uplift during salt doming and erosion at the surface. Such scenario is derived from the decompression model of extension-driven dewatering due to the strong difference in compressibility between rocks and fluids leading to overpressuring of pore fluids during denudation (Staude et al., 2009). In both scenarios, the ascent of the fluids would have been accompanied by a drop in temperature and pressure, which might have been a trigger for the precipitation of barite (Fig. 16). A drop of 200ºC to 100ºC (given a pressure of 500 bar) would result in the precipitation of up to 84 mg of barite per kg of fluid (Blount, 1977) assuming a 3M NaCl fluid based on our fluid inclusion data. Nevertheless, barite precipitation in burial settings has generally been attributed to mixing of fluids, because sulphate and barium (chloride) tend to not be transported together in fluids. Therefore, the ultimate trigger for barite precipitation may have been mixing of the ascending sulphate-rich brine (migrating along the fault) with a barium-rich fluid (most likely from formation fluids derived from interaction with barium-rich shales). Such conceptual model considers relatively fast advective fluid flow of sulphate-rich brines through fractures in the fault zone, which is typically episodic and cyclic linked with fault activity (Sibson, 1992) and involves elevated fluid pressure (Bons et al., 2012). This fault zone fluid flow alternates with episodes of relatively slow pervasive advective flow of barium-rich fluids through permeable formations (driven by convection in the aftermath of warm fluid migration along the fault) and important diffusional mass transport when fluid pressure is low (Wagner et al., 2010). Fluid mixing during fault activity in this case is most likely achieved by hydrodynamic dispersion (Bons et al., 2012).

7.4. Origin and formation process of calcite phases

Calcite precipitation can be triggered by several factors and is a common diagenetic product. In salt dome settings, it has been reported to form at about 70 to 100ºC from saline (5 to 20 wt% NaCl eq.) fluids (Morrison and Parry, 1986). It has also been postulated that CO_2 generated through degradation of organic matter (e.g., petroleum, methane) is an important source for calcite cement in carbonate cap rock (Bechtel et al., 1996). However, the latter mechanism is unlikely to explain the origin of calcite in Jebel Madar, since $\delta^{13}C$ is higher than -8‰ VPDB (Supplementary File Table 1), and the involvement of degradation of organic matter would lead to lower $\delta^{13}C$ values (Machel, 2001).

Similar to the stable isotope data of calcite in our study, Immenhauser et al. (2007) showed a decrease in $\delta^{18}O$ and especially $\delta^{13}C$ from fault zone calcite to macro-columnar calcite from Jebel Madar. Those authors interpreted that phreatic cave calcite in Jebel Madar formed by mixing of a saline hydrothermal fluid and a meteoric fresh water fluid (with incorporation of soil-derived light carbon). Also, Reuning et al. (2009) documented similar co-varying $\delta^{13}C$ and $\delta^{18}O$ trends from carbonate stringers of the surface-piercing salt domes from the Ghaba Salt Basin, and mixing of fluids with an additional source for lower $\delta^{13}C$ values linked to oxidized organic matter from liquid hydrocarbons consumed during sulphate reduction (Reuning et al., 2009). In addition to these previous studies in the area, we have documented the full assemblage of diagenetic components in the system found at the surface of the Jebel Madar dome and this is presented within a geospatial and structural framework.

The $^{87}Sr/^{86}Sr$ data also display distinct signatures for different diagenetic phases. The $^{87}Sr/^{86}Sr$ composition of fault zone calcite (0.7094) is close to that of Ara Group carbonate (0.7092) in Oman (Burns et al., 1994), whereas macro-columnar calcite has $^{87}Sr/^{86}Sr$ values of ≤ 0.7090, and the $^{87}Sr/^{86}Sr$ values of barite-associated calcite

and thin calcite vein samples range from 0.7092 up to 0.7110, indicating ^{87}Sr enrichment. The latter enrichment is interpreted to originate from incorporation of ^{87}Sr through liberation of Rb by aluminosilicate reactions (clay mineral reactions or K-feldspar dissolution) in the Haima Supergroup (Ramseyer et al., 2004), and this is consistent with the interpretation that the barite-forming fluids interacted with the Haima sandstones and the Ara anhydrite, as also derived from the sulphur isotope data.

The stable isotope and fluid inclusion data from both this work and previous work support formation of the diagenetic assemblage by mixing of fluids. We propose hereby that the high temperature saline end member is around 100ºC, as derived from the barite formation temperature (and supported by clumped isotope barite-associated calcite formation temperature), and that the low temperature meteoric end member is around 35ºC. We can then link the stable oxygen isotope data and the strontium isotope data to these end members and model mixing of those end members at different ratios (Appendix 1). For this model, we derive the $\delta^{18}O_{fluid}$ of +10.9‰ VSMOW based on $\delta^{18}O_{calcite}$ of -2.5‰ VPDB from barite-associated calcite formed at 100ºC, and $\delta^{18}O_{fluid}$ of -10.4‰ VSMOW based on $\delta^{18}O_{calcite}$ of -14.4‰ VPDB from macro-columnar calcite formed at 35ºC using the equation of Friedman and O'Neil (1977). This low temperature end member $\delta^{18}O_{fluid}$ signature is consistent with meteoric water from Southern Oman (Fleitmann et al., 2003). The stable oxygen isotopic signature of the macro-columnar calcite and reconstructed $\delta^{18}O_{fluid}$ are consistent with interpretations presented by Immenhauser et al. (2007) based on a fit between fluid inclusion δD values, the Southern Oman meteoric water line, $\delta^{18}O_{calcite}$, and derived temperature. The calculated high-temperature end member $\delta^{18}O_{fluid}$ value is consistent with basinal fluids that have dissolved Ara Group anhydrite based on the fact that $\delta^{18}O_{sulphate}$ in Neoproterozoic to Early Cambrian seawater is about

+14‰ VSMOW (Bottrell and Newton, 2006; Claypool et al., 1980; Longinelli and Craig, 1967).

The model of fluid mixing is presented using the end member data for temperature, $\delta^{18}O_{fluid}$, fluid inclusion salinity, and $^{87}Sr/^{86}Sr$ data (Fig. 17). Based on the mixing temperature and $\delta^{18}O_{fluid}$ values, the $\delta^{18}O_{calcite}$ values for different mixing ratios were reconstructed for this model (Fig. 17B). For temperature, $\delta^{18}O_{fluid}$, fluid inclusion salinity, and $^{87}Sr/^{86}Sr$ signatures, simple mixing using different fractions for the saline end member and the meteoric end member was applied (Appendix 1). For the $\delta^{13}C$ signature, the data show that no simple mixing of the two end member fluids is applicable. Here, the data indicate that carbon concentrations in the end member fluids were different, and a model taking account of 10 times higher concentration of carbon in the saline end member compared to the meteoric end member provides a good match for the observed data (Fig. 17B; Appendix 1). Our model assumes here that the signatures measured attribute to the signature of the fluids involved in the mixing model, and no local diffusion effects on the very small scale have been corrected for. Given the large scale of the diagenetic products, i.e. cm-sized crystals and meters to tens of meters wide fault zones, assuming predominantly fluid advective processes for mass transfer is justified for the interpretation of the calcite formation conditions and the relatively short time scale. However, diffusive processes played a role in the formation of thin calcite veins, and in the processes involved in the origin of the end member fluids (such as ^{87}Sr enrichment in sulphate-bearing fluids due to fluid-rock interaction).

In terms of the hydrodynamic feasibility of the mixing model, we would like to emphasize that our model does not involve simultaneously ascending and descending fluid migration along fault zones but is a dynamic model with two end member fluids. In Miocene time, episodes of ascending fluid migration occurred during fault activity and led to the formation of barite and subsequently barite-

associated calcite. These episodic events brought batches of saline fluid higher up along the fault zone, similar to the model of mobile hydrofractures suggested by Bons (2001). Meteoric fluids at the exposed surface caused weathering and erosion during uplift related to salt doming. With time, the exposed sedimentary package overlying the salt diapir became thinner, and hence meteoric fluids reached stratigraphically older formations. Saline fluids ascended during fault activity, whereas migration of meteoric fluids was probably more important during interseismic periods with low fluid pressure. The removal of the impermeable Nahr Umr Formation in the centre of the salt dome probably implied that no more ascending overpressured fluids were released along the faults. Instead, topographically-driven meteoric fluid flow became predominant along the exposed faults and in stratigraphic layers underlying the Nahr Umr Formation. These meteoric fluids mixed with the saline fluids that had ascended along the fault zones earlier.

The diversity of diagenetic products found in strata overlying salt domes is thus highly impacted by the origin of the end member fluids which likely involved interaction with anhydrite in the salt dome and overlying/surrounding carbonate and siliciclastic strata, and be influenced by other factors, such as the presence of organic rich strata or hydrocarbons. Mixing of fluids is a key mechanism triggering precipitation of minerals in salt dome settings. The barite-associated calcite formed by a predominant contribution of the saline end member fluid, whereas macro-columnar calcite formed by a dominant contribution of the meteoric fluid end member. Our model shows that the fault-zone calcite formed from around 50/50 to 90/10 ratio of meteoric/saline end member fluids (Fig. 17). The geochemical nature of the diagenetic products and their paragenesis reflect the structural evolution of the salt dome and related fluid flow with initially saline brines from interaction with the salt, and then a progressively larger contribution from meteoric fluids, probably linked with salt doming related uplift and infiltration of meteoric fluids along fault zones.

8. Conclusions

This study identified major barite and calcite diagenetic products in salt dome roof strata. Barite, barite-associated calcite, fault zone calcite and macro-columnar calcite occur all predominantly along NE-SW to NNE-SSW structures, which are interpreted to be templated by regional Precambrian basement faults, and no major diagenetic cementation is found along E-W faults. The spatial distribution of diagenetic products is not homogeneous among faults, and barite is concentrated in fault conjunctions and in the Hawk Valley fault zone parallel to, but away from, the main NE-SW graben structure of the Southwest Gully. The barite rosettes of cross-cutting, tabular, large crystals formed at about 100ºC in cavities linked to extensional fracturing during halokinesis. Barite sulphur isotope data indicate a mixed source with dissolved sulphate from the Ara Group and from the Haima Supergroup, the latter also contributing enriched ^{87}Sr to the diagenetic fluids. Salt doming resulted in fracturing of roof strata, creating pathways for fluid migration. Barite precipitation was probably triggered by mixing of an ascending sulphate-rich fluid and a barium-rich fluid. The transition of barite to barite-associated calcite precipitation could be controlled by a limitation in the barium supply. Mixing of the saline fluids with colder meteoric fluids has caused precipitation of fault zone calcite and macro-columnar calcite. The paragenetic sequence of the diagenetic products indicating an increase in the meteoric fluid component reflects the ongoing salt doming with uplift and extensional fault zone activity, and thus more extensive charging of meteoric fluids compared to the higher temperature saline fluids. Formation of the diagenetic products probably occurred over Miocene to Holocene time. The geochemical signatures measured in the diagenetic products fit a mixing model of a warm saline fluid and a colder meteoric fluid. Similar tectonic, hydrologic and fluid mixing evolution as derived for Jebel Madar can be expected in salt dome roof strata in other regions worldwide. Moreover, the methods (including structural diagenetic mapping) and modelling

techniques presented here can be applied in a range of other case studies that involve fluid migration along structures.

Acknowledgements

This research was funded by Qatar Petroleum, Shell and the Qatar Science and Technology Park (QSTP) and by the Stephen E. Laubach Research in Structural Diagenesis Award, granted by the Sedimentary Geology and the Structural Geology and Tectonics Divisions of the Geological Society of America. Field logistics were handled by Shuram. We acknowledge some field and lab work done by Janine Lahr at an early stage of this project. We would like to thank Emma Williams and Stanislav Strekopytov (ICP-AES) and Simon Davis (stable isotopes) for their help with various analytical techniques. Sulphur isotopes in barite were measured by IsoAnalytical. We thank Rosa Marimon from CCiT of the University of Barcelona for providing the oxygen isotope analyses in barite. We also thank Conxita Taberner for scientific discussions. We are very grateful to the associate editor Enrique Gomez-Rivas and the reviewers Mark Fischer and an anonymous reviewer for their valuable comments and suggestions which helped to improve the content and presentation of this manuscript.

References

Allen, P.A., 2007. The Huqf Supergroup of Oman: Basin development and context for Neoproterozoic glaciation. Earth-Science Reviews 84, 139-185.

Archer, S.G., Alsop, G.I., Hartley, A.J., Grant, N.T., Hodgkinson, R., 2012. Salt tectonics, sediments and prospectivity: an introduction, in: Alsop, G.I., Archer, S.G., Hartley, A.J., Grant, N.T., Hodgkinson, R. (Eds.), Salt Tectonics, Sediments and Prospectivity, pp. 1-6.

Badhe, K.V., Pandalai, H.S., 2015. Investigations on the Possible Re-equilibration of Aqueous Fluid Inclusions in Barite: A Study of Barite and Calcite from the Hutti Gold Deposit, Karnataka, India. Acta Geol. Sin.-Engl. Ed. 89, 715-725.

Balsamo, F., Clemenzi, L., Storti, F., Mozafari, M., Solum, J., Swennen, R., Taberner, C., Tueckmantel, C., 2016. Anatomy and paleofluid evolution of laterally restricted extensional fault zones in the Jabal Qusaybah anticline, Salakh arch, Oman. Geological Society of America Bulletin 128, 957-972.

778 Banerjee, D.M., Strauss, H., Bhattacharya, S.K., Kumar, V., Mazumdar, A., 1998.
779 Isotopic composition of carbonates and sulphates, potash mineralisation and basin
780 architecture of the Nagaur-Gangnagar evaporite basin (northwestern India) and their
781 implications on the Neoproterozoic exogenic cycle. Mineralogical Magazine 62A,
782 106-107.
783 Béchennec, F., Le Métour, J., Platel, J.P., Roger, J., 1993. Geological map of the
784 Sultanate of Oman. Ministry of Petroleum and Minerals, Sultanate of Oman.
785 Bechtel, A., Shieh, Y.N., Pervaz, M., Puttmann, W., 1996. Biodegradation of
786 hydrocarbons and biogeochemical sulfur cycling in the salt dome environment:
787 Inferences from sulfur isotope and organic geochemical investigations of the Bahloul
788 Formation at the Bou Grine Zn/Pb ore deposit, Tunisia. Geochimica Et
789 Cosmochimica Acta 60, 2833-2855.
790 Bertram, M.A., Cowen, J.P., 1997. Morphological and compositional evidence for
791 biotic precipitation of marine barite. Journal of Marine Research 55, 577-593.
792 Blount, C.W., 1977. Barite solubilities and thermodynamic quantities up to 300ºC and
793 1400 bars. American Mineralogist 62, 942-957.
794 Bons, P.D., 2001. The formation of large quartz veins by rapid ascent of fluids in
795 mobile hydrofractures. Tectonophysics 336, 1-17.
796 Bons, P.D., Elburg, M.A., Gomez-Rivas, E., 2012. A review of the formation of
797 tectonic veins and their microstructures. Journal of Structural Geology 43, 33-62.
798 Bottrell, S.H., Newton, R.J., 2006. Reconstruction of changes in global sulfur cycling
799 from marine sulfate isotopes. Earth-Science Reviews 75, 59-83.
800 Burns, S.J., Haudenschild, U., Matter, A., 1994. The strontium isotopic composition
801 of carbonates from the late Precambrian (approximate-to-560-540 Ma) Huqf Group of
802 Oman. Chemical Geology 111, 269-282.
803 Cai, C.F., Hu, G.Y., He, H., Li, J., Li, J.F., Wu, Y.S., 2005. Geochemical
804 characteristics and origin of natural gas and thermochemical sulphate reduction in
805 Ordovician carbonates in the Ordos Basin, China. Journal of Petroleum Science and
806 Engineering 48, 209-226.
807 Claringbould, J.S., Hyden, B.B., Sarg, J.F., Trudgill, B.D., 2013. Structural evolution
808 of a salt-cored, domed, reactivated fault complex, Jebel Madar, Oman. Journal of
809 Structural Geology 51, 118-131.
810 Claypool, G.E., Holser, W.T., Kaplan, I.R., Sakai, H., Zak, I., 1980. The age curves of
811 sulfur and oxygen isotopes in marine sulfate and their mutual interpretation.
812 Chemical Geology 28, 199-260.
813 Dehairs, F., Chesselet, R., Jedwab, J., 1980. Discrete suspended particles of barite
814 and the barium cycle in the open ocean. Earth and Planetary Science Letters 49,
815 528-550.
816 Demeny, A., Kele, S., Siklosy, Z., 2010. Empirical equations for the temperature
817 dependence of calcite-water oxygen isotope fractionation from 10 to 70 degrees C.
818 Rapid Communications in Mass Spectrometry 24, 3521-3526.
819 Dickson, J.A.D., 1966. Carbonate identification and genesis as revealed by staining.
820 Journal of Sedimentary Petrology 36, 491-505.
821 Droste, H., van Steenwinkel, M., 2004. Stratal geometries and patterns of platform
822 carbonates: The Cretaceous of Oman, in: Eberli, G.P., Masaferro, J.L., Sarg, J.F.R.
823 (Eds.), Seismic imaging of carbonate reservoirs and systems. AAPG Memoir, pp.
824 185-206.
825 Dunn, K., Daniel, E., Shuler, P.J., Chen, H.J., Tang, Y.C., Yen, T.F., 1999.
826 Mechanisms of surface precipitation and dissolution of barite: A morphology
827 approach. Journal of Colloid and Interface Science 214, 427-437.
828 Edgell, H.S., 1991. Proterozoic salt basins of the Persian Gulf area and their role in
829 hydrocarbon generation. Precambrian Research 54, 1-14.
830 Ericsson, J.B., McKean, H.C., Hooper, R.J., 1998. Facies and curvature controlled
831 3D fracture models in a Cretaceous carbonate reservoir, Arabian Gulf, in: Jones, G.,

Fischer, Q.J., Knipe, R.J. (Eds.), Faulting, fault sealing and fluid flow in hydrocarbon reservoirs. Geological Society of London, Special Publications, pp. 299-312.
Evans, D.G., Nunn, J.A., Hanor, J.S., 1991. Mechanisms driving groundwater-flow near salt domes. Geophysical Research Letters 18, 927-930.
Farzadi, P., 2006. The development of Middle Cretaceous carbonate platforms, Persian Gulf, Iran: constraints from seismic stratigraphy, well and biostratigraphy. Petroleum Geoscience 12, 59-68.
Feng, D., Roberts, H.H., 2011. Geochemical characteristics of the barite deposits at cold seeps from the northern Gulf of Mexico continental slope. Earth and Planetary Science Letters 309, 89-99.
Fleitmann, D., Burns, S.J., Neff, U., Mangini, A., Matter, A., 2003. Changing moisture sources over the last 330,000 yrs in northern Oman from fluid inclusion evidence in speleothems. Quaternary Research 60, 223-232.
Friedman, I., O'Neil, J.R., 1977. Chapter KK. Compilation of stable isotope fractionation factors of geochemical interest, in: Fleisher, M. (Ed.), Data of Geochemistry. United States Government Printing Office, Washington.
Gamboa, D., Alves, T.M., 2016. Bi-modal deformation styles in confined mass-transport deposits: Examples from a salt minibasin in SE Brazil. Marine Geology 379, 176-193.
Glennie, K.W., 2005. The geology of the Oman Mountains: an outline of their origin. Cambrian Printers, Great Britain, Aberstwyth.
Goldstein, R.H., Reynolds, T.J., 1994. Systematics of fluid inclusions in diagenetic minerals.
Gomez-Rivas, E., Bons, P.D., Koehn, D., Urai, J.L., Arndt, M., Virgo, S., Laurich, B., Zeeb, C., Stark, L., Blum, P., 2014. THE JABAL AKHDAR DOME IN THE OMAN MOUNTAINS: EVOLUTION OF A DYNAMIC FRACTURE SYSTEM. American Journal of Science 314, 1104-1139.
Gradmann, S., Beaumont, C., Ings, S.J., 2012. Coupled fluid flow and sediment deformation in margin-scale salt-tectonic systems: 1. Development and application of simple, single-lithology models. Tectonics 31.
Greinert, J., Bollwerk, S.M., Derkachev, A., Bohrmann, G., Suess, E., 2002. Massive barite deposits and carbonate mineralization in the Derugin Basin, Sea of Okhotsk: precipitation processes at cold seep sites. Earth and Planetary Science Letters 203, 165-180.
Griffith, E.M., Paytan, A., 2012. Barite in the ocean - occurrence, geochemistry and palaeoceanographic applications. Sedimentology 59, 1817-1835.
Hallager, W.S., Ulrich, M.R., Kyle, J.R., Price, P.E., Gose, W.A., 1990. Evidence for episodic basin dewatering in salt-dome cap rocks. Geology 18, 716-719.
Hanor, J.S., 1994. Origin of saline fluids in sedimentary basins, in: Parnell, J. (Ed.), Geofluids: Origin, Migration and Evolution of Fluids in Sedimentary Basins. Geological Society Special Publications, pp. 151-174.
Hanor, J.S., 2000. Barite-celestine geochemistry and environments of formation. Sulfate Minerals - Crystallography, Geochemistry and Environmental Significance 40, 193-275.
Holzbecher, E., Kohfahl, C., Mazurowski, M., Bacik, A., Dobies, M., Schneider, M., 2010. The Sensitivity of Thermohaline Groundwater Circulation to Flow and Transport Parameters: A Numerical Study Based on Double-Diffusive Convection above a Salt Dome. Transport in Porous Media 83, 771-791.
Hudec, M.R., Jackson, M.P.A., 2007. Terra infirma: Understanding salt tectonics. Earth-Science Reviews 82, 1-28.
Immenhauser, A., Dublyansky, Y.V., Verwer, K., Fleitmann, D., Pashenko, S.E., 2007. Textural, elemental, and isotopic characteristics of Pleistocene phreatic cave deposits (Jabal Madar, Oman). Journal of Sedimentary Research 77, 68-88.

Jackson, C.A.L., Lewis, M.M., 2016. Structural style and evolution of a salt-influenced rift basinmargin; the impact of variations in salt composition and the role of polyphase extension. Basin Research 28, 81-102.
Jackson, M.P.A., Vendeville, B.C., 1994. Regional extension as a geologic trigger for diapirism. Geological Society of America Bulletin 106, 57-73.
John, C.M., Vandeginste, V., Jourdan, A.-L., Kluge, T., Davis, S., Sena, C., Hönig, M., Beckert, J., 2014. Carbonate reservoir analogues and clumped isotopes: How combined geometries and geochemistry of outcrops help reservoir management in the Middle East. IPTC Conference Paper, 17256.
Kusakabe, M., Robinson, B.W., 1977. Oxygen and sulfur isotope equilibriq in BaSO4-HSO4-H2O system from 110 to 350-degrees-C and applications. Geochimica Et Cosmochimica Acta 41, 1033-1040.
Longinelli, A., Craig, H., 1967. Oxygen-18 variations in sulfate ions in sea water and saline lakes. Science (New York, N.Y.) 156, 56-59.
Loosveld, R.J.H., Bell, A., Terken, J.J.M., 1996. The tectonic evolution of interior Oman. GeoArabia 1, 28-50.
Machel, H.G., 2001. Bacterial and thermochemical sulfate reduction in diagenetic settings - old and new insights. Sedimentary Geology 140, 143-175.
Mann, A., Hanna, S.S., 1990. The tectonic evolution of pre-Permian rocks, Central and Southeastern Oman Mountains, in: Robertson, A.H.F., Searle, M.P., Ries, A.C. (Eds.), The Geology and Tectonics of the Oman Region. Geological Society Special Publication, London, pp. 307-325.
Marchev, P., Downes, H., Thirlwall, M.F., Mortiz, R., 2002. Small-scale variations of 87Sr/86Sr isotope composition of barite in the Madjarovo low-sulphidation epithermal system, SE Bulgaria: implications for sources of Sr, fluid fluxes and pathways of the ore-forming fluids. Mineralium Deposita 37, 669-677.
Mattes, B.W., Morris, S.C., 1990. Carbonate evaporite deposition in the late Precambrian - early Cambrian Ara Formation of southern Oman, in: Robertson, A.H.F., Searle, M.P., Ries, A.C. (Eds.), Geology and Tectonics of the Oman Region. Geological Society of London, Special Publications, pp. 617-636.
Mattos, N.H., Alves, T.M., Omosanya, K.O., 2016. Crestal fault geometries reveal late halokinesis and collapse of the Samson Dome, Northern Norway: Implications for petroleum systems in the Barents Sea. Tectonophysics 690, 76-96.
Morrison, S.J., Parry, W.T., 1986. Formation of carbonate-sulfate veins associated with copper ore-deposits from saline basin brines, Lisbon Valley, Utah - fluid inclusion and isotopic evidence. Economic Geology 81, 1853-1866.
Mount, V.S., Crawford, R.I.S., Bergman, S.C., 1998. Regional structural style of the central and southern Oman Mountains: Jebel Akhdar, Saih Hatat, and the Northern Ghaba Basin. GeoArabia 3, 475-490.
Mozafari, M., Swennen, R., Balsamo, F., Clemenzi, L., Storti, F., El Desouky, H., Vanhaecke, F., Tueckmantel, C., Solum, J., Taberner, C., 2015. Paleofluid evolution in fault-damage zones: evidence from fault-fold interaction events in the Jabal Qusaybah anticline (Adam Foothills, North Oman). Journal of Sedimentary Research 85, 1525-1551.
Omosanya, K.d.O., Alves, T.M., 2013. Ramps and flats of mass-transport deposits (MTDs) as markers of seafloor strain on the flanks of rising diapirs (Espirito Santo Basin, SE Brazil). Marine Geology 340, 82-97.
Paytan, A., Kastner, M., Campbell, D., Thiemens, M.H., 2004. Seawater sulfur isotope fluctuations in the cretaceous. Science 304, 1663-1665.
Pe-Piper, G., Piper, D.J.W., Zhang, Y.X., Chavez, I., 2015. Diagenetic barite and sphalerite in middle Mesozoic sandstones, Scotian Basin, as tracers for basin hydrology. AAPG Bulletin 99, 1281-1313.
Peters, J.M., Filbrandt, J., Grotzinger, J., Newall, M., Shuster, M., Al-Siyabi, H., 2003. Surface-piercing salt domes in the interior North Oman, and their significance for the Ara carbonate 'stringer' hydrocarbon play. GeoArabia 8, 1-40.

Quinta, A., Tavani, S., Roca, E., 2012. Fracture pattern analysis as a tool for constraining the interaction between regional and diapir-related stress fields: Poza de la Sal Diapir (Basque Pyrenees, Spain), in: Alsop, G.I., Archer, S.G., Hartley, A.J., Grant, N.T., Hodgkinson, R. (Eds.), Salt Tectonics, Sediments and Prospectivity, pp. 521-532.

Ramseyer, K., Amthor, J.E., Spötl, C., Terken, J.J.M., Matter, A., Vroon-ten Hove, M., Borgomano, J.R.F., 2004. Impact of basin evolution, depositional environment, pore water evolution and diagenesis on reservoir-quality of Lower Paleozoic Haima Supergroup sandstones, Sultanate of Oman. GeoArabia 9, 107-138.

Ranganathan, V., 1992. Basin dewatering near salt domes and formation of brine plumes. Journal of Geophysical Research-Solid Earth 97, 4667-4683.

Ranganathan, V., Hanor, J.S., 1989. Perched brine plumes above salt domes and dewatering of geopressured sediments. Journal of Hydrology 110, 63-86.

Rees, C.E., Jenkins, W.J., Monster, J., 1978. Sulfur isotopic composition of ocean water sulfate. Geochimica Et Cosmochimica Acta 42, 377-381.

Reuning, L., Schoenherr, J., Heimann, A., Urai, J.L., Littke, R., Kukla, P.A., Rawahi, Z., 2009. Constraints on the diagenesis, stratigraphy and internal dynamics of the surface-piercing salt domes in the Ghaba Salt Basin (Oman): A comparison to the Ara Group in the South Oman Salt Basin. GeoArabia 14, 83-120.

Sarkar, A., Nunn, J.A., Hanor, J.S., 1995. Free thermohaline convection beneath allochthonous salt sheets - an agent for salt dissolution and fluid-flow in Gulf-Coast sediments. Journal of Geophysical Research-Solid Earth 100, 18085-18092.

Sassen, R., Cole, G.A., Drozd, R., Roberts, H.H., 1994. Oligocene to Holocene hydrocarbon migration and salt-dome carbonates, northern Gulf-of-Mexico. Marine and Petroleum Geology 11, 55-65.

Saunders, J.A., Thomas, R.C., 1996. Origin of 'exotic' minerals in Mississippi salt dome cap rocks: Results of reaction-path modeling. Applied Geochemistry 11, 667-676.

Schoenherr, J., Reuning, L., Kukla, P.A., Littke, R., Urai, J.L., Siemann, M., Rawahi, Z., 2009. Halite cementation and carbonate diagenesis of intra-salt reservoirs from the Late Neoproterozoic to Early Cambrian Ara Group (South Oman Salt Basin). Sedimentology 56, 567-589.

Schoenherr, J., Schléder, Z., Urai, J.L., Littke, R., Kukla, P.A., 2010. Deformation mechanicsms of deeply buried and surface-piercing Late Pre-Cambrian to Early Cambrian Ara Salt from interior Oman. International Journal of Earth Sciences 99, 1007-1025.

Schroder, S., Schreiber, B.C., Amthor, J.E., Matter, A., 2003. A depositional model for the terminal Neoproterozoic Early Cambrian Ara Group evaporites in south Oman. Sedimentology 50, 879-898.

Schroder, S., Schreiber, B.C., Amthor, J.E., Matter, A., 2004. Stratigraphy and environmental conditions of the terminal Neoproterozoic-Cambrian period in Oman: evidence from sulphur isotopes. J. Geol. Soc. 161, 489-499.

Shikazono, N., 1994. Precipitation mechanisms of barite in sulfate-sulfide deposits in back-arc basins. Geochimica Et Cosmochimica Acta 58, 2203-2213.

Sibson, R.H., 1992. Fault-valve behavior and the hydrostatic lithostatic fluid pressure interface. Earth-Science Reviews 32, 141-144.

Smith, A.P., Fischer, M.P., Evans, M.A., 2012. Fracture-controlled palaeohydrology of a secondary salt weld, La Popa Basin, NE Mexico, in: Alsop, G.I., Archer, S.G., Hartley, A.J., Grant, N.T., Hodgkinson, R. (Eds.), Salt Tectonics, Sediments and Prospectivity, pp. 107-130.

Souissi, F., Sasst, R., Dandurand, J.-L., Bouhlel, S., Ben Hamdal, S., 2007. Fluid inclusion microthermometry and rare earth element distribution in the celestites of the Jebel Doghra ore deposit (Dome Zone, northern Tunisia): towards a new genetic model. Bulletin De La Societe Geologique De France 178, 459-471.

994 Staude, S., Bons, P.D., Markl, G., 2009. Hydrothermal vein formation by extension-
995 driven dewatering of the middle crust: An example from SW Germany. Earth and
996 Planetary Science Letters 286, 387-395.
997 Strauss, H., Banerjee, D.M., Kumar, V., 2001. The sulfur isotopic composition of
998 Neoproterozoic to early Cambrian seawater - evidence from the cyclic Hanseran
999 evaporites, NW India. Chemical Geology 175, 17-28.
1000 Terken, J.M.J., Frewin, N.L., Indrelid, S.L., 2001. Petroleum systems of Oman:
1001 charge timing and risks. AAPG Bulletin 85, 1817-1845.
1002 Thirlwall, M.F., 1991. Long-term reproducibility of multicollector Sr and Nd isotope
1003 ratio analysis. Chemical Geology 94, 85-104.
1004 Tombros, S.F., Seymour, K.S., Williams-Jones, A.E., Zhai, D., Liu, J., 2015. Origin of
1005 a barite-sulfide ore deposit in the Mykonos intrusion, cyclades: Trace element,
1006 isotopic, fluid inclusion and raman spectroscopy evidence. Ore Geology Reviews 67,
1007 139-157.
1008 Torres, M.E., Bohrmann, G., Dube, T.E., Poole, F.G., 2003. Formation of modern
1009 and Paleozoic stratiform barite at cold methane seeps on continental margins.
1010 Geology 31, 897-900.
1011 Ulrich, M.R., Bodnar, R.J., 1988. Systematics of stretching of fluid inclusions. 2.
1012 Barite at 1-atm confining pressure. Economic Geology 83, 1037-1046.
1013 Vandeginste, V., John, C.M., Manning, C., 2013a. Interplay between depositional
1014 facies, diagenesis and early fractures in the Early Cretaceous Habshan Formation,
1015 Jebel Madar, Oman. Marine and Petroleum Geology 43, 489-503.
1016 Vandeginste, V., John, C.M., van de Flierdt, T., Cosgrove, J.W., 2013b. Linking
1017 process, dimension, texture and geochemistry in dolomite geobodies: a case study
1018 from Wadi Mistal (northern Oman). AAPG Bulletin 97, 1181-1207.
1019 Vandeginste, V., Swennen, R., Gleeson, S.A., Ellam, R.M., Osadetz, K., Roure, F.,
1020 2006. Development of secondary porosity in the Fairholme carbonate complex
1021 (southwest Alberta, Canada). Journal of Geochemical Exploration 89, 394-397.
1022 Vandeginste, V., Swennen, R., Gleeson, S.A., Ellam, R.M., Osadetz, K., Roure, F.,
1023 2009. Thermochemical sulphate reduction in the Upper Devonian Cairn Formation of
1024 the Fairholme carbonate complex (South-West Alberta, Canadian Rockies): evidence
1025 from fluid inclusions and isotopic data. Sedimentology 56, 439-460.
1026 Vendeville, B.C., 2005. Salt tectonics driven by sediment progradation: Part I -
1027 Mechanics and kinematics. AAPG Bulletin 89, 1071-1079.
1028 Wagner, T., Boyce, A.J., Erzinger, J., 2010. FLUID-ROCK INTERACTION DURING
1029 FORMATION OF METAMORPHIC QUARTZ VEINS: A REE AND STABLE
1030 ISOTOPE STUDY FROM THE RHENISH MASSIF, GERMANY. American Journal of
1031 Science 310, 645-682.
1032 Wagner, T., Kirnbauer, T., Boyce, A.J., Fallick, A.E., 2005. Barite-pyrite
1033 mineralization of the Wiesbaden thermal spring system, Germany: a 500-kyr record
1034 of geochemical evolution. Geofluids 5, 124-139.
1035 Wang, T., Yang, C., Ma, H., Daemen, J.J.K., Wu, H., 2015. Safety evaluation of gas
1036 storage caverns located close to a tectonic fault. Journal of Natural Gas Science and
1037 Engineering 23, 281-293.
1038 Warren, J.K., 2000. Evaporites, brines and base metals: low-temperature ore
1039 emplacement controlled by evaporite diagenesis. Australian Journal of Earth
1040 Sciences 47, 179-208.
1041 Williams, M.D., Ranganathan, V., 1994. Ephemeral thermal and solute plumes
1042 formed by upwelling groundwaters near salt domes. Journal of Geophysical
1043 Research-Solid Earth 99, 15667-15681.
1044 Wilson, A., Ruppel, C., 2007. Salt tectonics and shallow subseafloor fluid convection:
1045 models of coupled fluid-heat-salt transport. Geofluids 7, 377-386.
1046 Yang, C., Wang, T., Li, Y., Yang, H., Li, J., Qu, D.a., Xu, B., Yang, Y., Daemen,
1047 J.J.K., 2015. Feasibility analysis of using abandoned salt caverns for large-scale
1048 underground energy storage in China. Applied Energy 137, 467-481.

Yin, H., Groshong, R.H., Jr., 2007. A three-dimensional kinematic model for the deformation above an active diapir. Aapg Bulletin 91, 343-363.
Yin, H., Zhang, J., Meng, L., Liu, Y., Xu, S., 2009. Discrete element modeling of the faulting in the sedimentary cover above an active salt diapir. Journal of Structural Geology 31, 989-995.

Figure captions

Figure 1. (A) Geological map of northern Oman, simplified after Béchennec et al. (1993). (B) Geological map of Jebel Madar, modified after Claringbould et al. (2013).

Figure 2. Overview of stratigraphic units outcropping in Jebel Madar.

Figure 3. Field photographs of barite occurrences. Lens cap (diameter of 58 mm) as scale. (A) Lekhwair Formation limestone host rock is cross-cut by vein that contains barite (Bar) at the sides and lighter coloured calcite (Cc) in the center. (B) Barite tabular crystals (white arrow indicates one) are dispersed within host rock, forming fan-shape or radiating patterns (black arrow). (C) Barite, forming layers with some radiating patterns. Note the high porosity. (D) Rosettes of cross-cutting tabular barite crystals (black arrow).

Figure 4. Microphotographs taken under polarized light (A, C, E) and CL (B, D, F), with A & B, C & D and E & F being pairs of images that show the exact same region. Scale bar is 500 µm. (A & B) Non-luminescent barite laths and dark orange, dull luminescent calcite with some lighter orange luminescent calcite zones. (C & D) Coarse fault zone calcite with darker and lighter orange, dull luminescent zonations. (E & F) Macro-columnar calcite, which is mainly non-luminescent, with a few thin, orange, dull luminescent zonations.

1079 Figure 5. Field photographs of calcite cements. Lens cap (5.8 cm) as scale. (A)
1080 Relatively thin calcite veins within host rock. (B) Calcite cement (C) in between
1081 tabular barite (B). (C) Striated fault plane with coarse calcite cementation. Person
1082 (1.7 m) as scale. (D) Macro-columnar calcite with transparent and reddish coloured
1083 zones. Marker (14 cm) as scale. (E) Macro-columnar calcite in radiating pattern. Note
1084 that this calcite cement also occurs along a fault. (F) Calcite rosettes present in the
1085 same fault zone as the macro-columnar calcite shown in panel C.
1086
1087 Figure 6. Field photographs of cross-cutting of calcite cement phases. Lens cap (5.8
1088 cm) as scale. (A) Calcite (C) associated with barite (B) cross-cut by reddish brown silt
1089 layer. (B) Cross-cutting calcite phases and reddish brown silt with speleothems of
1090 macro-columnar calcite. (C-E) Fault zones with several white calcite, transparent,
1091 and reddish, macro-columnar calcite vein generations.
1092
1093 Figure 7. Satellite image of Jebel Madar with indication of the occurrence of different
1094 phases. Most squares on the map represent a set of samples at that locality. Empty
1095 quarters of the square indicate that the specific corresponding phases were not
1096 sampled and thus, generally absent. This mapping mainly aimed at reconstructing
1097 the distribution of barite and major calcite occurrences; hence, the distribution of
1098 small calcite veins is underrepresented on this figure.
1099
1100 Figure 8. Rose diagrams of structures that contain thin calcite veins, barite-
1101 associated calcite, fault zone calcite and macro-columnar calcite. Bin size is 15º and
1102 the circles indicate the number of data points (e.g. barite-associated calcite has
1103 seven data points which fall in the N30-45 bin).
1104
1105 Figure 9. Crossplot of sulphur isotope versus oxygen isotope signature for barite.
1106 Each data point represents a measurement from a powder sample drilled from an

individual hand sample (33 data points from 33 different hand samples, Supplementary File Table 1). Apart from two outliers, the data form a cluster. The rough linear correlation between the two proxies is not significant (R^2 = 0.44; two outliers excluded). The $\delta^{18}O$ is high compared to marine barite and also $\delta^{34}S$ is relatively high, but similar to that of Late Neoproterozoic to Early Cambrian anhydrite.

Figure 10. Crossplot of stable carbon and oxygen isotopic composition of limestone and defined calcite types. Each data point represents a different hand sample, but in several occasions multiple hand samples were taken from zones in the same large calcite fault zone, fracture or cavern. The distribution shows a clear trend towards lower values for both $\delta^{13}C$ and $\delta^{18}O$ from barite-associated calcite and thin calcite veins to fault zone calcite to macro-columnar calcite.

Figure 11. Crossplot of stable oxygen and strontium isotopic composition of limestone and defined calcite types. The distribution shows a decrease in average strontium isotopic ratio from barite-associated calcite and thin calcite veins to fault zone calcite and to macro-columnar calcite. The strontium isotopic composition of the Ara Group carbonate in Oman is based on Burns et al. (1994).

Figure 12. Major and minor element contents in defined calcite types. (A) Crossplot of Mg versus Sr content, showing a weak positive correlation. (B) Box and whisker plot of Mn content, showing a decreasing average value from barite-associated calcite to thin calcite veins to fault zone calcite to macro-columnar calcite, similar to the trend observed in the stable isotope signature. Note though that the data range for the different calcite types overlap.

1133 Figure 13. Photomicrographs of fluid inclusions. (A) Primary single-phase fluid
1134 inclusions in cluster in barite, and also secondary fluid inclusion trails are present. (B)
1135 Primary single-phase and two-phase fluid inclusions in cluster barite, and also thin
1136 trails of very small secondary fluid inclusions. (C) Single-phase fluid inclusions
1137 interpreted as primary in origin, in barite-associated calcite. (D) Primary isolated
1138 single-phase fluid inclusions in macro-columnar calcite.
1139
1140 Figure 14. (A) Plot of homogenization temperature versus salinity from fluid inclusion
1141 measurements in barite. (B) Crossplot of stable oxygen isotope composition of calcite
1142 versus salinity of fluid inclusions (both primary and secondary) measured in the
1143 respective calcite sample.
1144
1145 Figure 15. Paragenetic sequence of diagenetic events.
1146
1147 Figure 16. Interpreted structural and paleohydrological evolution (in four time steps)
1148 presented for a transect through the southwestern part of Jebel Madar. The exact
1149 location and extent of the Ara salt diapir is uncertain at this location since seismic
1150 sections are only available from the area surrounding Jebel Madar (Claringbould et
1151 al., 2013). An early Paleocene time step is not presented here given the maximum
1152 stress direction was NW-SE at that time which is almost parallel to the orientation of
1153 the presented transect. The NNE-SSW to NE-SW faults displayed on the transect
1154 were not active in early Paleocene time and no fluid flow is expected along those
1155 faults at that time. However, the E-W faults developed as dextral strike-slip faults in
1156 early Paleocene.
1157
1158 Figure 17. Mixing model indicating geochemical signatures. (A) Mixing model of
1159 saline (17 wt% NaCl eq) end member fluid at 100ºC, $\delta^{18}O_{fluid}$ of +10.9‰ VSMOW and

$^{87}Sr/^{86}Sr$ of 0.71023 and meteoric (0 wt% NaCl eq) end member fluid at 35ºC, $\delta^{18}O_{fluid}$ of -10.4‰ VSMOW and $^{87}Sr/^{86}Sr$ of 0.70884. Note the slightly irregular temperature scale (compared to the meteoric fluid fraction scale) due to the different heat capacity of saline versus meteoric fluid. (B) Mixing model of the same two fluid end members as presented in A showing reconstructed $\delta^{18}O_{calcite}$ and $\delta^{13}C_{calcite}$ (considering 10 times higher carbon content in the saline end member compared to the meteoric end member).

Appendix 1.

The mixing calculations are based on a linear mixing model of two end member components for the determination of salinity, $^{87}Sr/^{86}Sr$ and $\delta^{18}O_{fluid}$, through the following equation:

$$V_{mix} = F_1 V_1 + (1 - F_1) V_2$$

where V_{mix} is the calculated signature of the mixture, F_1 is the meteoric fluid fraction, V_1 is the signature of the meteoric fluid end member and V_2 is the signature of the saline end member fluid.

For the determination of the temperature of the mixed fluid, we need to take account of the different heat capacities of the meteoric end member fluid and the saline end member fluid, through the following equation:

$$T_{mix} = \frac{F_1}{F_1 + \frac{C_{v2}}{C_{v1}}(1 - F_1)} T_1 + \frac{\frac{C_{v2}}{C_{v1}}(1 - F_1)}{F_1 + \frac{C_{v2}}{C_{v1}}(1 - F_1)} T_2$$

where T_{mix} is the calculated temperature of the mixture, F_1 is the meteoric fluid fraction, T_1 is the temperature of the meteoric fluid end member, T_2 is the temperature of the saline end member fluid, C_{v1} is the heat capacity of the meteoric end member fluid and C_{v2} is the heat capacity of the saline end member fluid.

Similarly, the stable carbon isotopic composition of the mixture can be calculated by taking account of the different carbon content in the end member fluid:

$$\delta^{13}C_{mix} = \frac{F_1}{F_1 + \frac{c_2}{c_1}(1-F_1)}\delta^{13}C_1 + \frac{\frac{c_2}{c_1}(1-F_1)}{F_1 + \frac{c_2}{c_1}(1-F_1)}\delta^{13}C_2$$

where $\delta^{13}C_{mix}$ is the calculated stable carbon isotope composition of the mixture, F_1 is the meteoric fluid fraction, $\delta^{13}C_1$ is the stable carbon isotope composition of the meteoric fluid end member, $\delta^{13}C_2$ is the stable carbon isotope composition of the saline end member fluid, c_1 is the carbon content of the meteoric end member fluid and c_2 is the carbon content of the saline end member fluid.

Supplementary File Table 1

Table 1. Carbon, oxygen and strontium isotope data of host rock, thin calcite veins, barite-associated calcite, fault zone calcite and macro-columnar calcite. Details of latitude and longitude of sampling are also presented.

Supplementary File Table 2

Table 2. Geochemical elemental data of host rock, thin calcite veins, barite-associated calcite, fault zone calcite, intermediate calcite and macro-columnar calcite. Details of latitude and longitude of sampling are presented as well.

Supplementary File Table 3

Table 3. Fluid inclusion data of barite-associated calcite, fault zone calcite, and macro-columnar calcite. Tfm: temperature of observed first melting, Tm ice: temperature of final melting of ice, Th: homogenization temperature.

Supplementary File Figure 18.

1209 Figure 18. Histograms of stable carbon and oxygen isotope data measured in the
1210 different calcite types, and the fluid inclusion final melting temperature of ice data in
1211 the different diagenetic types.
1212
1213
1214
1215

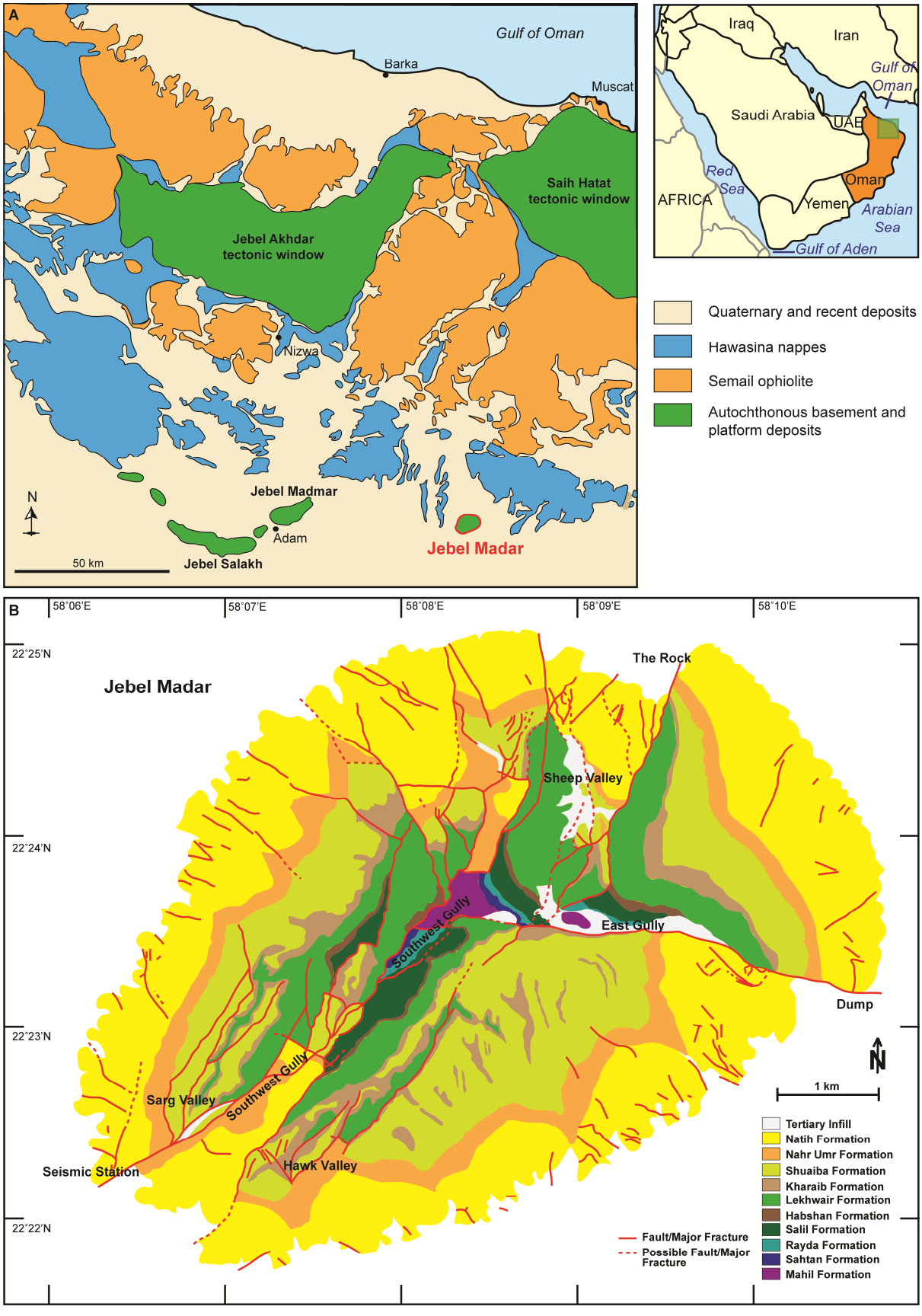

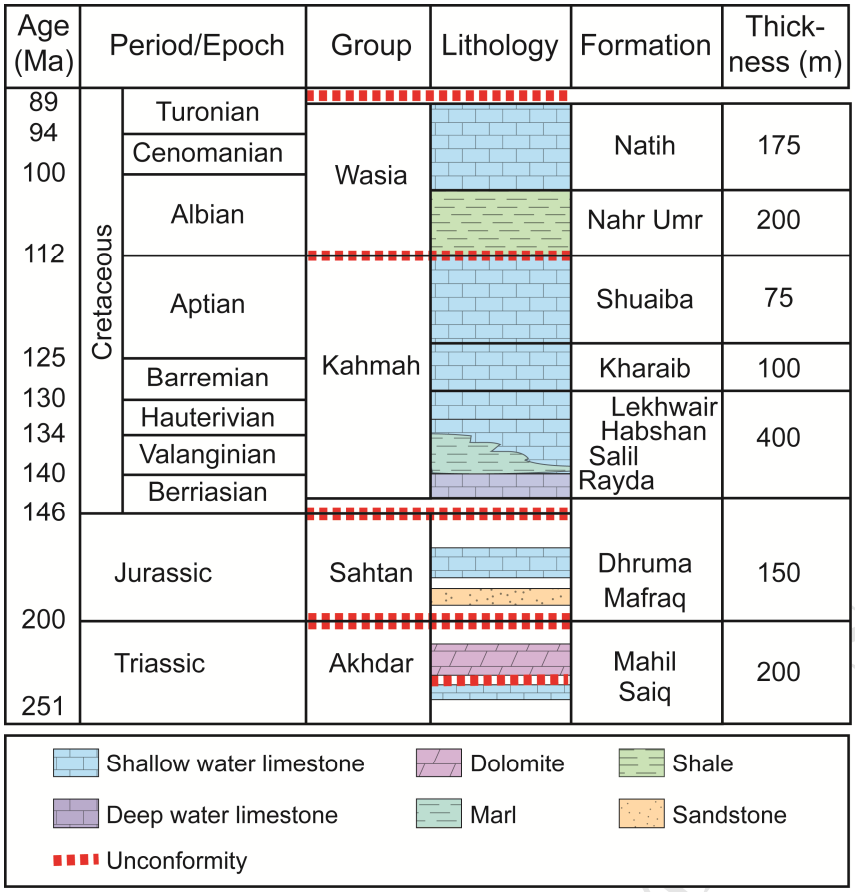

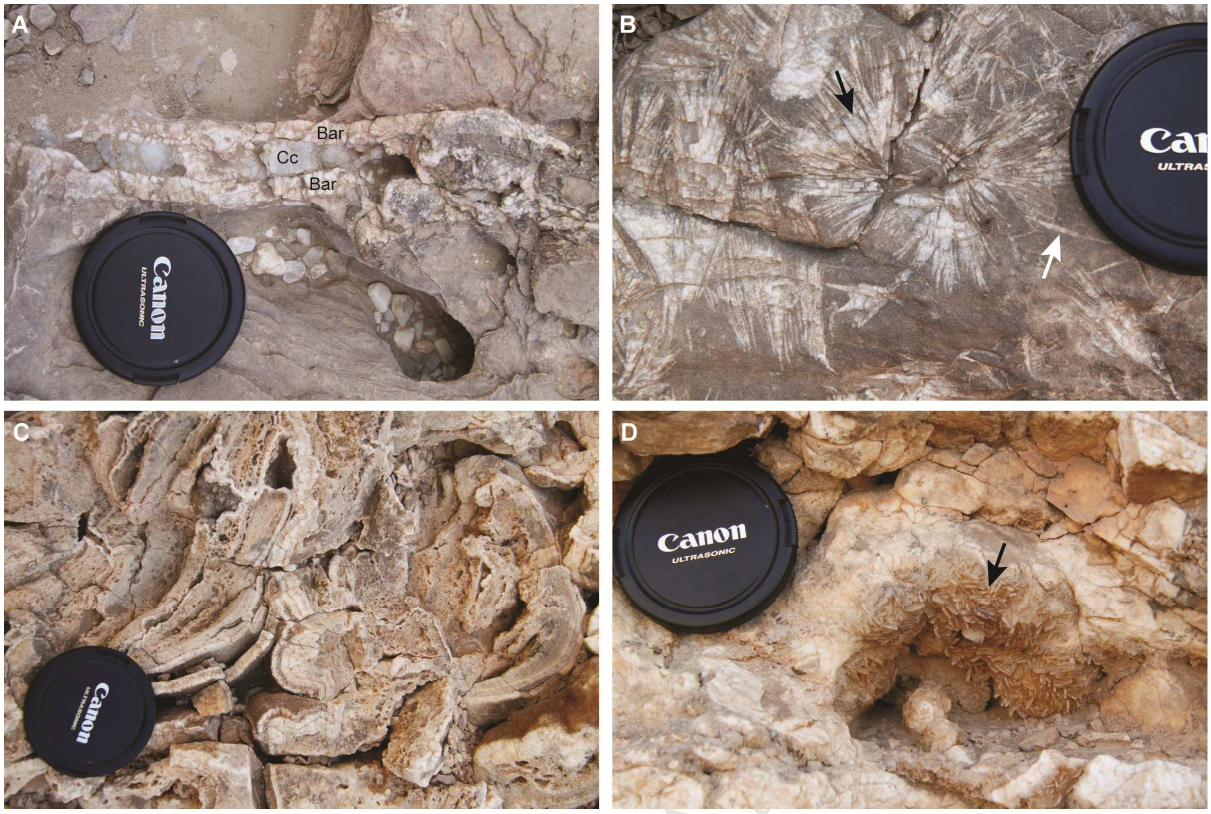

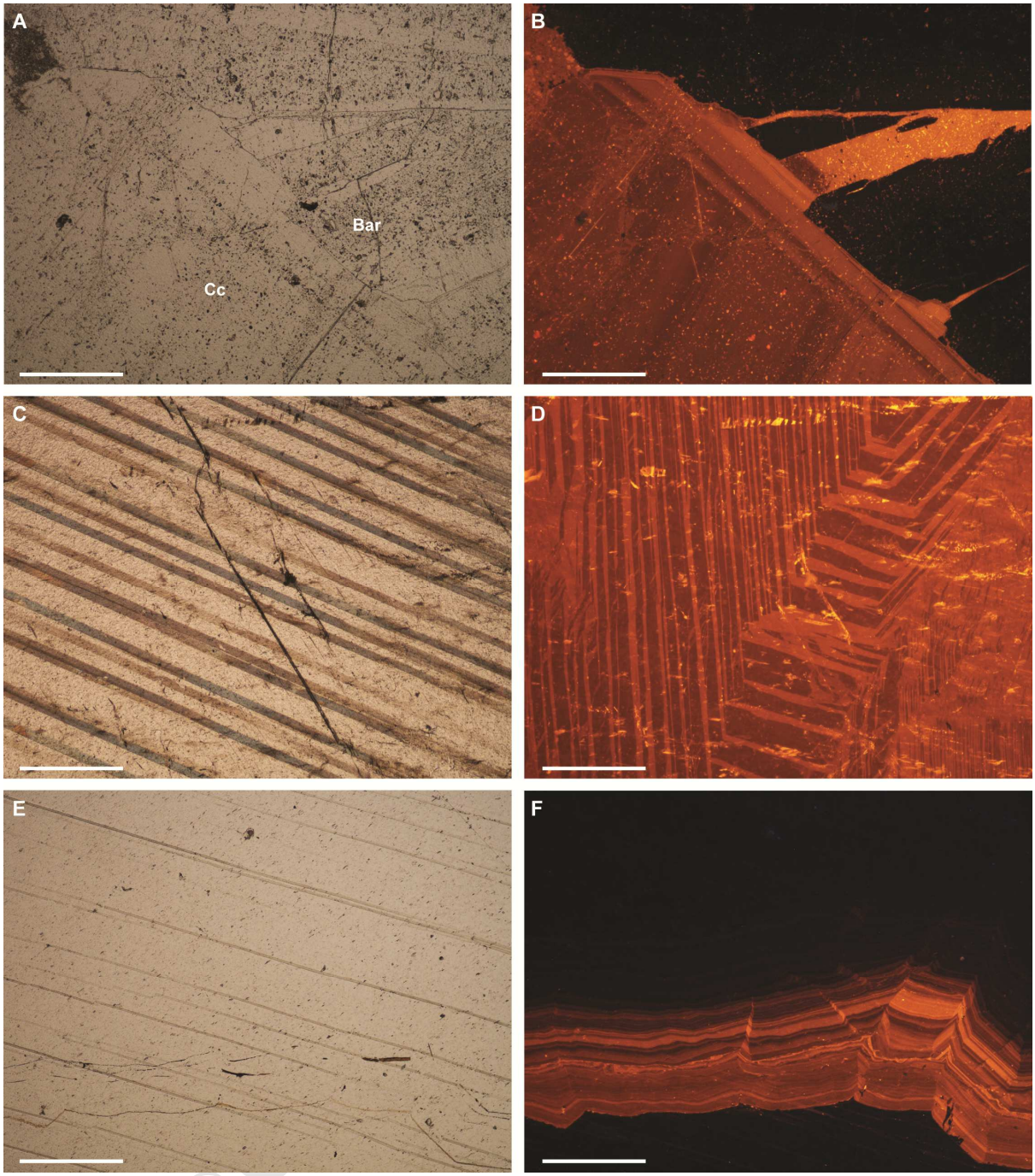
A
Bar
Cc
B
C
D
E
F

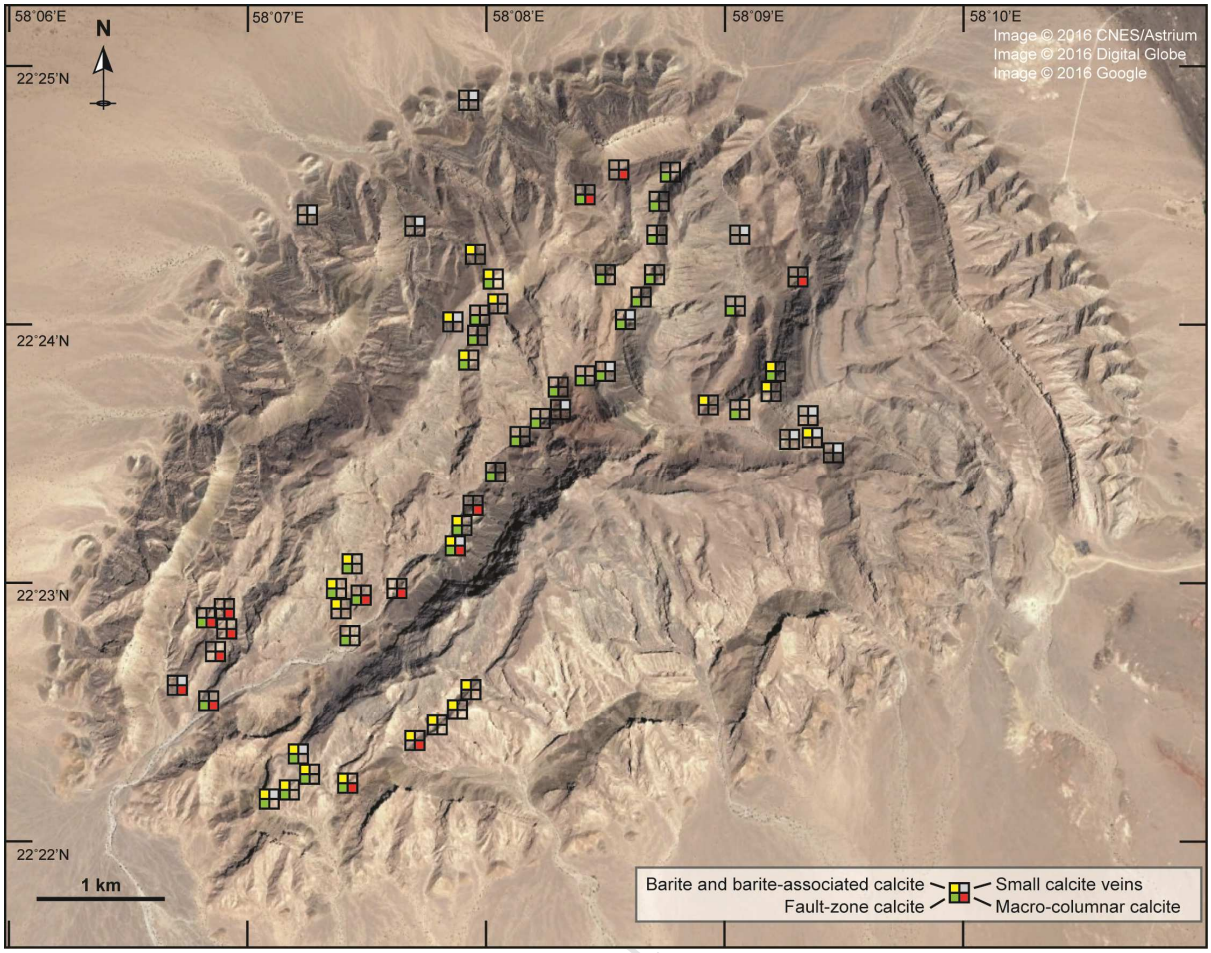

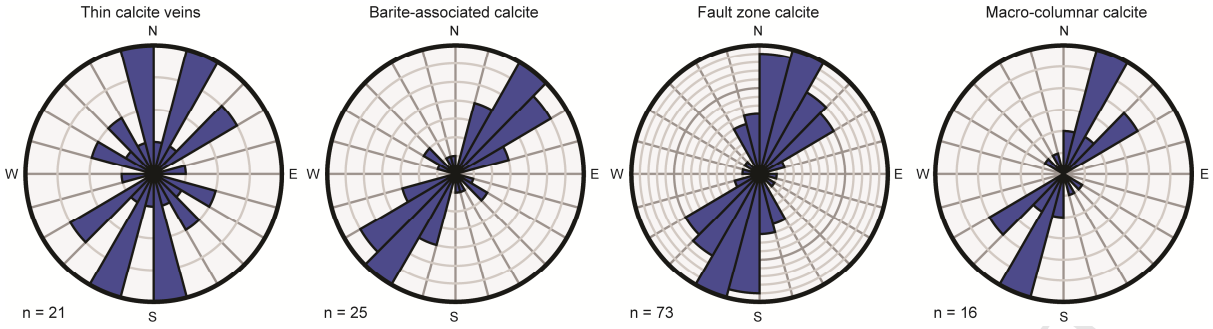

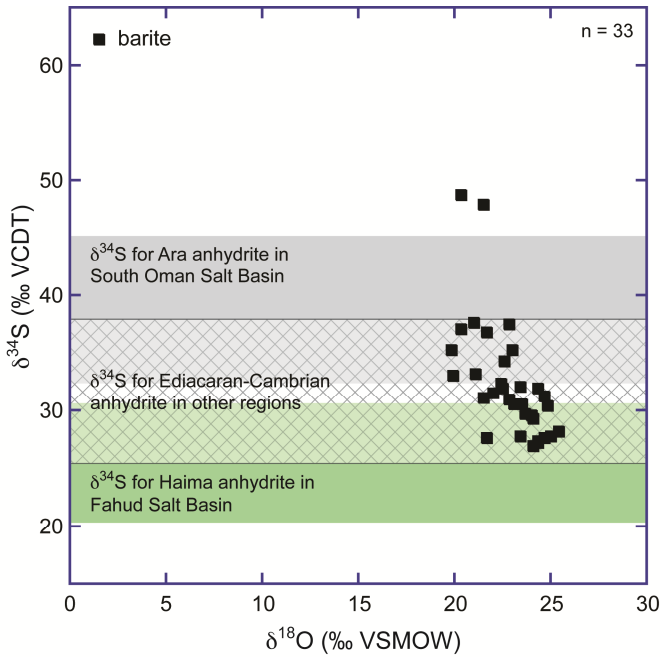

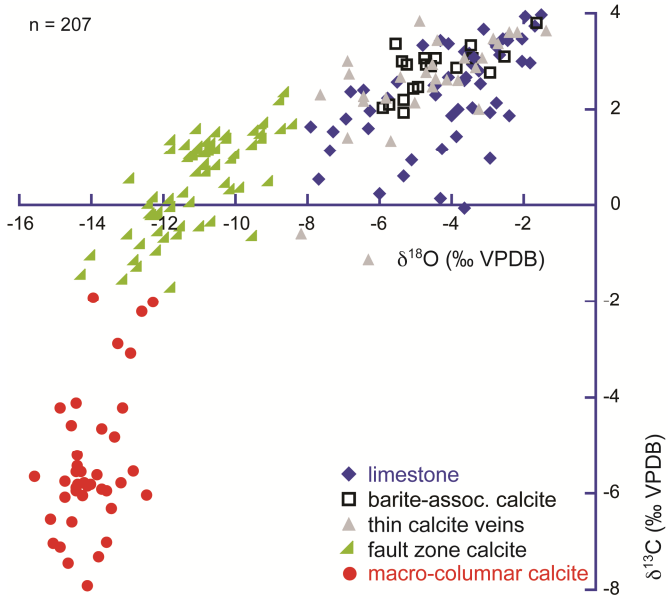

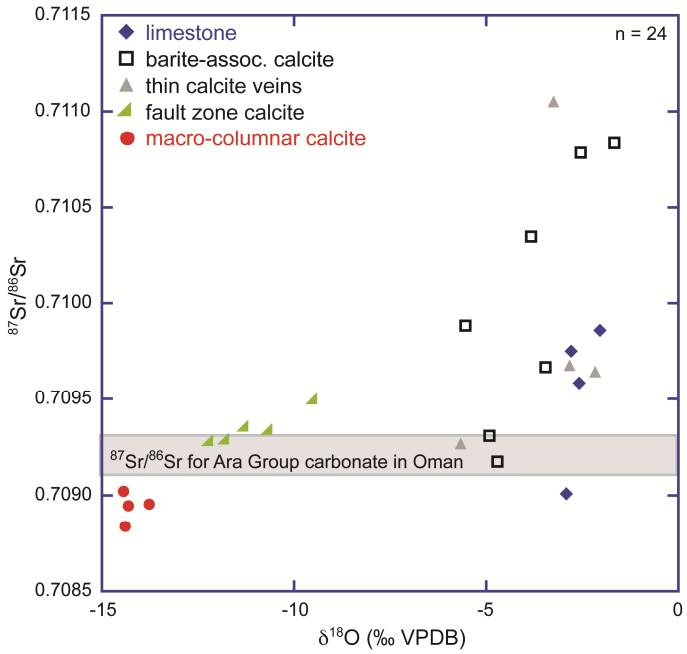

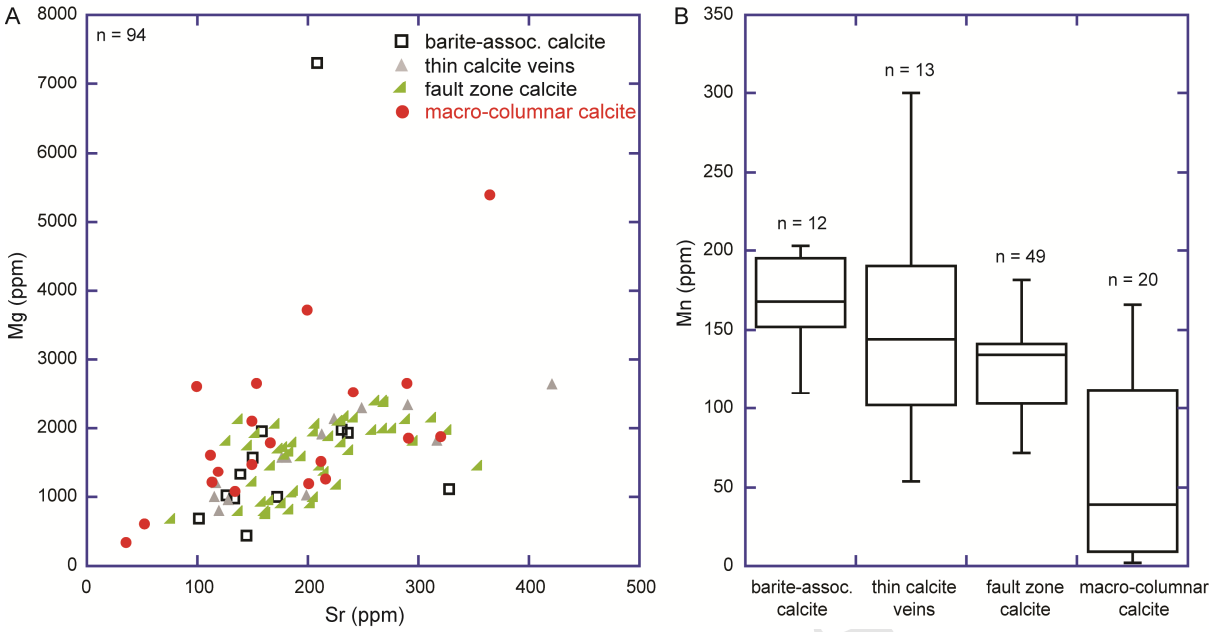

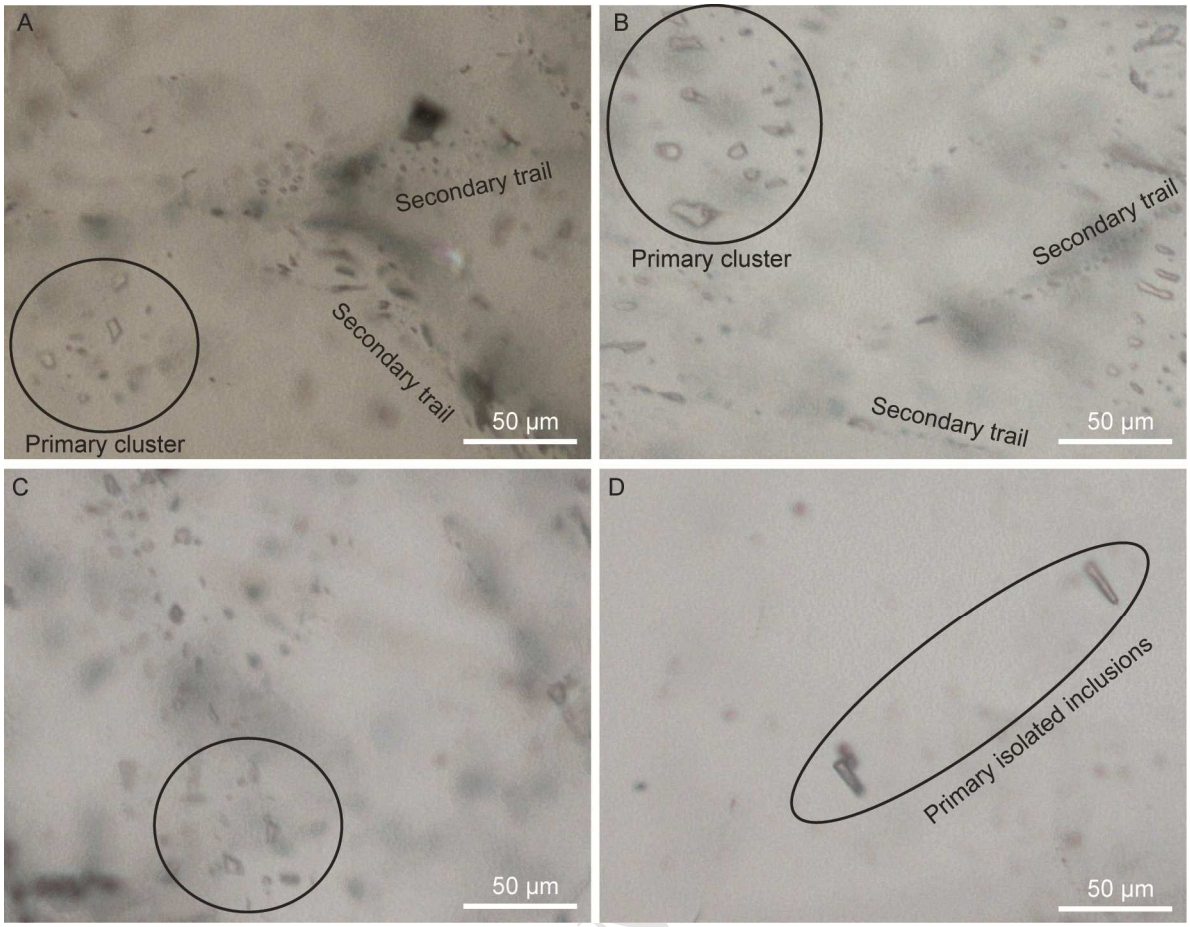

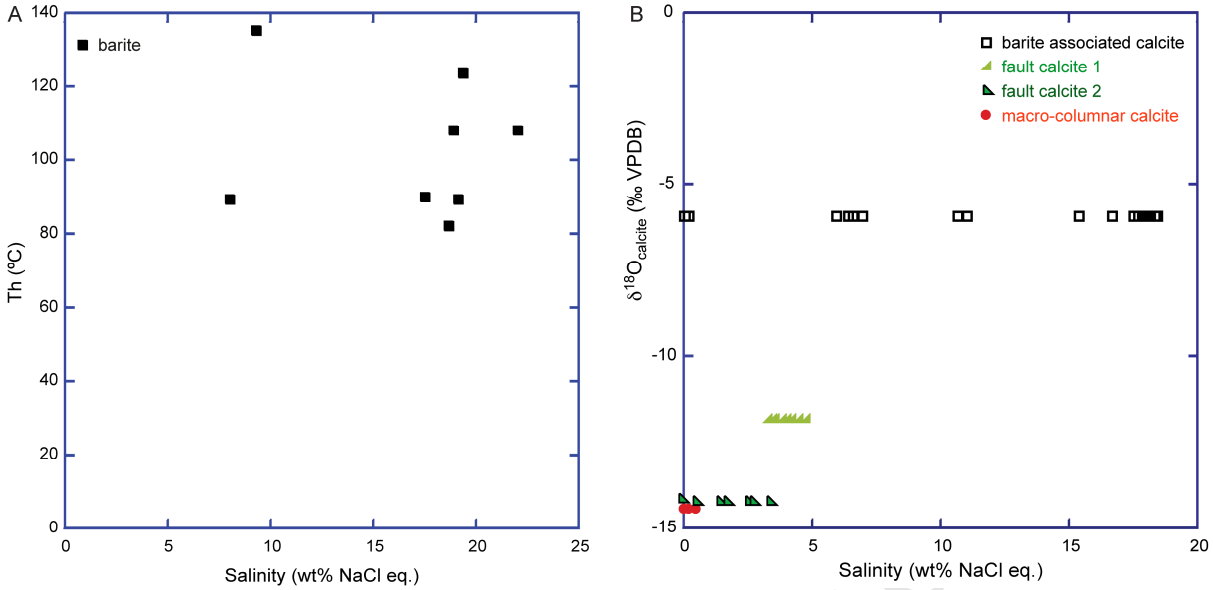

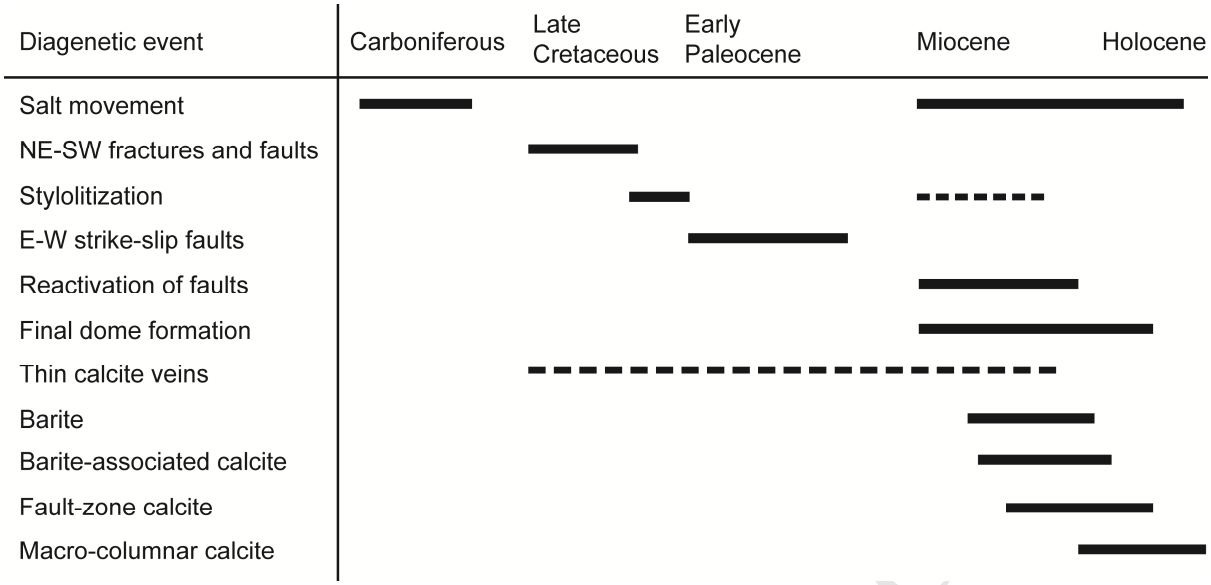

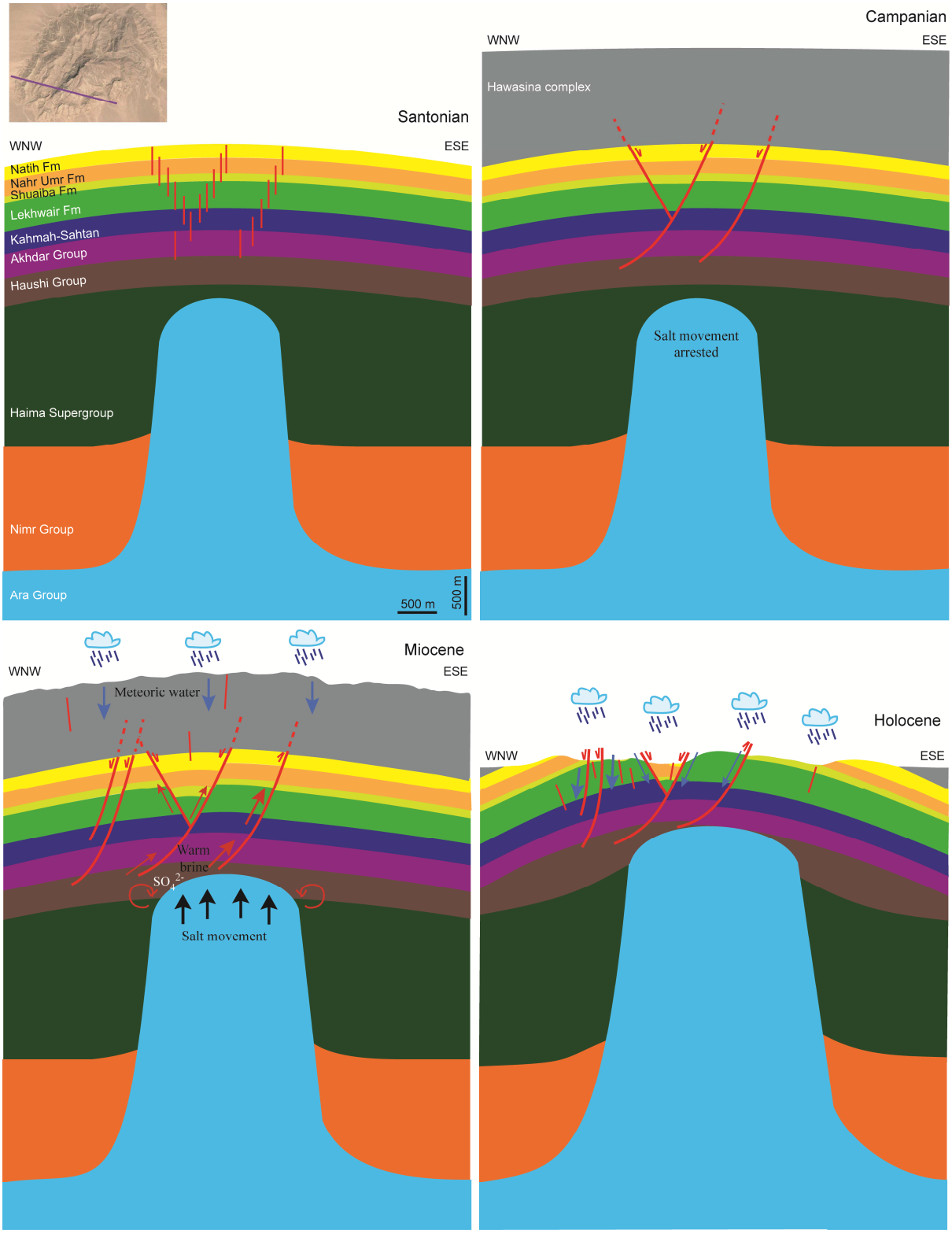
Santonian
WNW
ESE
Natih Fm
Nahr Umr Fm
Shuaiba Fm
Lekhwair Fm
Kahmah-Sahtan
Akhdar Group
Haushi Group
Haima Supergroup
Nimr Group
Ara Group
500 m
500 m
Campanian
WNW
ESE
Hawasina complex
Salt movement arrested
Miocene
WNW
ESE
Meteoric water
Warm brine
SO_4^{2-}
Salt movement
Holocene
WNW
ESE

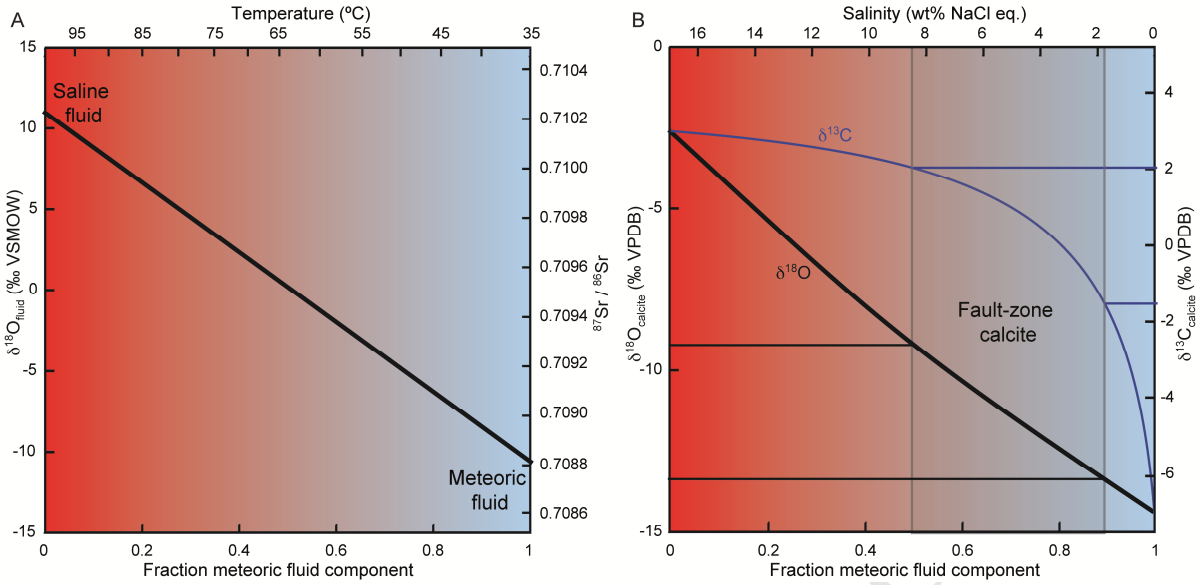

Highlights

Diagenesis in salt dome roof strata: barite - calcite assemblage in Jebel Madar, Oman

- The spatial distribution of diagenetic phases in a salt dome in Oman is presented.
- Clear link between structural evolution and fluid flow in salt dome roof strata.
- Barite sulfate source comes from Ara Group evaporite and Haima Supergroup layers.
- Diagenetic products occur mainly along NE-SW to ENE-WSW faults and fractures.
- Warm saline fluids mix progressively with meteoric fluids during Miocene to Pleistocene.